Water Resources Research

RESEARCH ARTICLE
10.1029/2024WR037549

Self-Potential Tomography Preconditioned by Particle Swarm Optimization—Application to Monitoring Hyporheic Exchange in a Bedrock River

Scott J. Ikard[1], Kenneth C. Carroll[2], Scott C. Brooks[3], Dale F. Rucker[4], Gladisol Smith-Vega[2], and Aubrey Elwes[2]

[1]U.S. Geological Survey, Oklahoma-Texas Water Science Center, Austin, TX, USA, [2]New Mexico State University, College of Agricultural, Consumer, and Environmental Sciences, Las Cruces, NM, USA, [3]Oak Ridge National Laboratory, Oak Ridge, TN, USA, [4]hydroGEOPHYSICS, Inc., Tucson, AZ, USA

Key Points:

- Hyporheic exchange flows in East Fork Poplar Creek occur along fault lines and fractures in the limestone bedrock riverbed
- Self-potential tomography is preconditioned by particle swarm optimization and applied to synthetic models and self-potential monitoring data
- Inverse models image electrical sources attributed to groundwater flow along a known fault in the flood plain of East Fork Poplar Creek

Supporting Information:

Supporting Information may be found in the online version of this article.

Correspondence to:

S. J. Ikard,
sikard@usgs.gov

Citation:

Ikard, S. J., Carroll, K. C., Brooks, S. C., Rucker, D. F., Smith-Vega, G., & Elwes, A. (2024). Self-potential tomography preconditioned by particle swarm optimization—application to monitoring hyporheic exchange in a Bedrock River. *Water Resources Research*, *60*, e2024WR037549. https://doi.org/10.1029/2024WR037549

Received 19 MAR 2024
Accepted 16 OCT 2024

Author Contributions:

Conceptualization: Scott J. Ikard, Kenneth C. Carroll, Scott C. Brooks
Data curation: Scott J. Ikard, Dale F. Rucker
Formal analysis: Scott J. Ikard, Dale F. Rucker
Funding acquisition: Scott J. Ikard, Kenneth C. Carroll
Investigation: Scott J. Ikard, Kenneth C. Carroll, Scott C. Brooks, Dale F. Rucker, Gladisol Smith-Vega, Aubrey Elwes
Methodology: Scott J. Ikard, Kenneth C. Carroll, Dale F. Rucker

Abstract A self-potential (SP) data-inversion algorithm was developed and tested on an analytical model of electrical-potential profile data attributed to single and multiple polarized electrical sources. The developed algorithm was then validated by an application to SP-monitoring field data measured on the floodplain of East Fork Poplar Creek, Oak Ridge, Tennessee, to image electrical sources in areas conducive to preferential flow into the flood plain from the bedrock-lined riverbed. The algorithm combined stochastic source-localization by particle-swarm-optimization (PSO) of electrical sources characterized by simplified geometries with source tomography by regularized weighted least-squares minimization of a quadratic objective function. Prior information was incorporated by preconditioning the tomography algorithm by PSO results. Variable percentages of random noise were added to analytical-model data to evaluate the algorithm performance. Results indicated that true parameters of single-source models were inverted and approximated with small residual error, whereas inversion of analytical-model data representing multiple electrical sources accurately approximated the locations of the sources but miscalculated some parameters because of the non-uniqueness of the inverse-model solution. Source tomography applied to analytical model data during testing produced a spatially continuous parameter field that identified the locations of point-scale synthetic dipole sources of electrical current flow with varying degrees of accuracy depending on the prior information incorporated into the tomography. When applied to SP-monitoring field data, the algorithm imaged electrical sources within a known fault that intersects the bedrock riverbed and flood plain of East Fork Poplar Creek and depicted dynamic electrical conditions attributed to hyporheic exchange.

Plain Language Summary A self-potential (SP)-data inversion method was developed and tested on synthetic models of electrical-potential data and electrical-potential field data acquired by monitoring voltages through time at multiple locations on the flood plain of a river flowing over a bedrock aquifer. The SP-data inversion method (a) calculates horizontal electrical-potential profile data over buried electrical sources with user-defined properties, (b) finds the locations of unknown electrical sources of electrical-potential data by particle swarm optimization (PSO), (c) performs electrical-source imaging using the locations of the sources determined by PSO as a guide, and (d) enables real-time monitoring of water exchange between a river and a bedrock aquifer. The results obtained by applying the inversion method to SP-monitoring data depict transient electrical changes in a bedrock aquifer that are affected by changes in streamflow and attributed to water exchange between the river and aquifer along a fault.

1. Introduction

The hyporheic zone plays a role in hydrological and ecological functioning of bedrock rivers (Bencala, 2005; Cardenas & Gooseff, 2008; Findlay, 1995; Harvey & Gooseff, 2015; Krause et al., 2011; White, 1993). A bedrock river is defined herein as a stream flowing over a bedrock aquifer, which may or may not be lined with a thin layer of alluvial sediment on the streambed and adjacent flood plain. Understanding the temporal dynamics of small-scale hyporheic-zone processes in bedrock rivers is essential for understanding watershed function and preserving river ecosystems. The methodologies available for investigating the hyporheic zone in alluvial rivers are of limited use in bedrock rivers (Kalbus et al., 2006; Krause et al., 2011) because fracture networks and karst features create more complex groundwater-flow patterns and render the hyporheic zone less directly accessible. The relative inaccessibility of the hyporheic zone in bedrock rivers has been identified as the source of a knowledge

Project administration: Scott J. Ikard, Kenneth C. Carroll
Resources: Scott J. Ikard, Kenneth C. Carroll, Scott C. Brooks, Dale F. Rucker, Gladisol Smith-Vega, Aubrey Elwes
Software: Scott J. Ikard, Dale F. Rucker
Supervision: Scott J. Ikard, Kenneth C. Carroll
Validation: Scott J. Ikard
Visualization: Scott J. Ikard, Dale F. Rucker
Writing – original draft: Scott J. Ikard
Writing – review & editing: Scott J. Ikard, Kenneth C. Carroll, Scott C. Brooks, Dale F. Rucker

gap in the scientific literature (Chow et al., 2021; Kennedy, 2017; Oxtobee and Novakowski, 2002, 2003; Tinkler and Wohl, 1998).

Self-potential (SP) methods offer a broad range of contributions for investigating the hyporheic zone in bedrock rivers and assisting in mitigating the perceived knowledge gap (Jouniaux et al., 2009; Linde et al., 2011; Revil and Jardani, 2013; Revil et al., 2017; Valois et al., 2018; Ikard et al., 2018, 2021a, 2021b, 2023a, 2023b). SP methods include land-based and waterborne mapping and monitoring of naturally occurring electrical-potential signals that arise from subsurface electrical current flows. Primary electrical current flows are created by fluid, heat, and ion fluxes along hydraulic, thermal, electrochemical, and ionic-concentration gradients. Secondary electrical current flows are attributed to heterogeneities in hydraulic and electrical properties of geologic materials that result in spatial gradients of cross-coupling coefficients, and also are attributed to seismoelectric effects (Barde-Cabusson et al., 2021; Ikard et al., 2012; Ikard & Revil, 2014; Mitchell, 1991; Nyquist and Corry, 2002; Revil et al., 2013; Revil and Linde, 2006; Revil and Mahardika, 2013; Rittgers et al., 2013; Sill, 1983). The importance of primary and secondary electrical current flows on the total flux of electrical current depends on the relative magnitude of the fluid, heat, or ionic flux and the corresponding cross-coupling conductivity coefficient (Sheffer and Oldenburg, 2007).

Interpreting hyporheic zone processes from land-based or waterborne self-potential (WaSP) data requires forward and inverse modeling of the electrical-potential field created by primary and secondary electrical current flows. Whereas the SP forward problem calculates the electrical-potential field produced by a collection of known or assumed electrical-current sources, the SP inverse problem consists of calculating a unique model of the geospatial distribution of buried electrical-current sources from measured electrical-potential data. The inverse model minimizes residual error between measured electrical-potential data and inverse-modeled (simulated) electrical-potential data and optimizes a trade-off between residual error and model complexity to prevent overfitting inherent noise in the data.

Many SP-data inversion algorithms are published in the scientific literature given the nearly 200 years of theoretical and applied development of the method in the geophysical, geological, and hydrological sciences (Barde-Cabusson et al., 2021). The variety of published SP inversion algorithms includes gradient-based algorithms such as linear and nonlinear least-squares optimization (Jardani et al., 2007a, 2008; Minsley et al., 2007a, 2007b; Essa et al., 2008; Martínez-Pagán et al., 2010; Richards et al., 2010; Rittgers et al., 2013; Soueid Ahmed et al., 2013), global-search algorithms such as simulated annealing and particle swarm optimization (Biswas, 2016; Biswas & Sharma, 2015; Di Maio et al., 2019; Elhussein, 2021; Gobashy et al., 2020; Göktürkler & Balkaya, 2012; Luo et al., 2023; Sharma and Biswas, 2013; Srivastava et al., 2014; Sungkono, 2020; Sungkono and Warnana, 2018), and a multitude of other algorithms and approaches to SP-data inversion (Haas et al., 2013; Jardani et al., 2007b, 2009; Mendonça, 2008; Mehanee, 2022, to list a few). Although gradient-based algorithms are generally more mature for highly parameterized geophysical inverse problems compared to global search algorithms, there are two main disadvantages of gradient-based algorithms: (a) they require calculations of partial derivatives of the forward model with respect to the model parameters to construct the Jacobian or Hessian matrices, and (b) their convergence upon global minima of the optimized objective function, as opposed to localized minima in parameter space, is not guaranteed and depends upon the selection of the initial parameter values (Luo et al., 2023).

Alternative to gradient-based algorithms, swarm-intelligence algorithms such as PSO are a variety of global-search algorithms that have become a focus of research in geophysical inverse problems and have received much recent attention for inversion of potential-fields data (gravity, magnetic, and SP data) (Essa, 2019, 2020; Essa and Elhussein, 2018, 2020; Fernández-Martínez et al., 2010; Göktürkler & Balkaya, 2012; Luo et al., 2023; Monteiro Santos, 2010; Pekşen et al., 2011; Shi and Eberhart, 1998; Singh and Biswas, 2016). PSO optimizes a geophysical problem by randomly and iteratively repositioning a population of candidate solutions (particles) within a large parameter search space to seek a best solution based on a specified measure of data misfit. The PSO algorithm is robust in the presence of data noise, provides greater convergence speed and accuracy compared to other popular global-search algorithms (Göktürkler & Balkaya, 2012), and attempts to solve the SP inverse problem as a stochastic sampling problem to overcome the tendencies of gradient-based algorithms to converge upon local minima of the objective function (Yuan et al., 2009).

Despite the abundance of SP-data inversion algorithms published in the scientific literature, demonstrations of inversions of SP data to study transient hyporheic exchange in a bedrock river are currently (as of 2024)

nonexistent. An SP-data inversion method is therefore developed in this work from a combination of global-search and gradient-based algorithms and validated through applications to synthetic geoelectrical models and SP monitoring data measured along two intersecting electrode arrays installed into the flood plain of a bedrock river to monitor electrical sources in the bedrock aquifer attributed to hyporheic exchange. PSO is applied to an analytical model of electrical potential data attributed to electrically polarized current sources characterized by arbitrary simple geometric shapes to perform source localization. Gradient-based source tomography is then performed using source-localization results to reduce noise in the inverted data and precondition the objective function with prior information about the locations and intensities of stochastic electrical-current sources. The demonstrated methods are intended to produce an SP-monitoring and data-inversion method for temporal SP monitoring and characterization of a known or suspected hydrologic exchange feature.

2. The Self-Potential Forward Problem

The classical SP forward problem consists of solving the governing groundwater-flow (Equation 1) (Anderson et al., 2015) and electrostatic (Equation 2) (Revil et al., 2012) partial differential equations for spatial distributions of Darcy velocity ($\mathbf{u}$; m s^{-1}) (Equation 1), and electrical potential (φ; mV) (Equation 2), respectively. The forward-model geometry is an imperfect representation of reality that is commonly defined and parameterized by the electrical resistivity distribution (ρ; ohm-m) (Equation 2) obtained from an electrical resistivity tomography survey. Electrical and hydraulic boundary conditions and parameterizations are assigned to the forward-model geometry and the Darcy velocity and electrical-potential distributions are calculated on a finite-difference grid or finite-element mesh incorporating the resistivity and hydraulic conductivity distributions.

$$\nabla \cdot \mathbf{u} = \mathrm{Q_s} \tag{1}$$

$$\nabla \cdot \left(\rho^{-1} \nabla \varphi\right) = \nabla \cdot \mathbf{j_s} \tag{2}$$

The governing partial differential equations are coupled by petrophysical relations between electrical and hydraulic material and fluid properties shown in Equations 3 and 4 (Bolève et al., 2007; Ikard et al., 2023c; Jardani et al., 2007a, 2008). At the differential control-volume scale, groundwater sources and sinks ($\mathrm{Q_s}$; s^{-1}) generate primary sources of positive and negative electric charge (Crespy et al., 2008; Sheffer and Oldenburg, 2007; Vasconcelos et al., 2014). The advection of electric charges in the diffuse band of the electrical double layer generates streaming current ($\mathbf{j_s}$; A m^{-2}), quantified by the product of Darcy velocity and excess (volumetric) charge density ($\widehat{\mathrm{Q_v}}$; C m^{-3}) as shown in Equation 3. Groundwater sources and sinks therefore alter the volumetric current density ($\nabla \cdot \mathbf{j_s}$; in A m^{-3}), which is the source-term in the electrostatic equation (Bolève et al., 2007; Revil et al., 2005; Revil and Leroy, 2001, 2004). The excess (volumetric) charge density in Equation 3 has been shown to be well approximated by the empirical function of intrinsic permeability (k_i; m^2) given in Equation 4 (Jardani et al., 2007a, 2008; Jardani & Revil, 2009).

$$\mathbf{j_s} = \widehat{\mathrm{Q_v}}\,\mathbf{u} \tag{3}$$

$$\log_{10}\widehat{\mathrm{Q_v}} = -9.2 - 0.82\log_{10}k_i \tag{4}$$

As an alternative to forward modeling the coupled groundwater-flow and electrostatic partial-differential equations, SP anomalies can be calculated along a horizontal profile from an analytical model of electrical potential attributed to electrically polarized current sources that have simple geometric shapes such as spheres, horizontal or vertical semi-infinite cylinders, or inclined planes (Babu & Rao, 1988; Banerjee, 1971; Bhattacharya & Roy, 1981; Biswas & Sharma, 2015; Essa, 2019, 2020; Essa & Elhussein, 2017; Essa et al., 2008; El-Kaliouby & Al-Garni, 2009; Gobashy et al., 2020; Monteiro Santos, 2010; Rao and Babu, 1983; Roudsari and Beitollahi, 2013; Sundararajan et al., 1998; Yüngül, 1950). The analytical-model equation describing electrical-potential anomalies $\varphi(x)$ (mV) any point x along a horizontal profile above an assemblage of electrical-current sources is given in Equation 5. This model is applicable to multiple electrical sources with spherical and cylindrical shapes positioned within a homogeneous half-space.

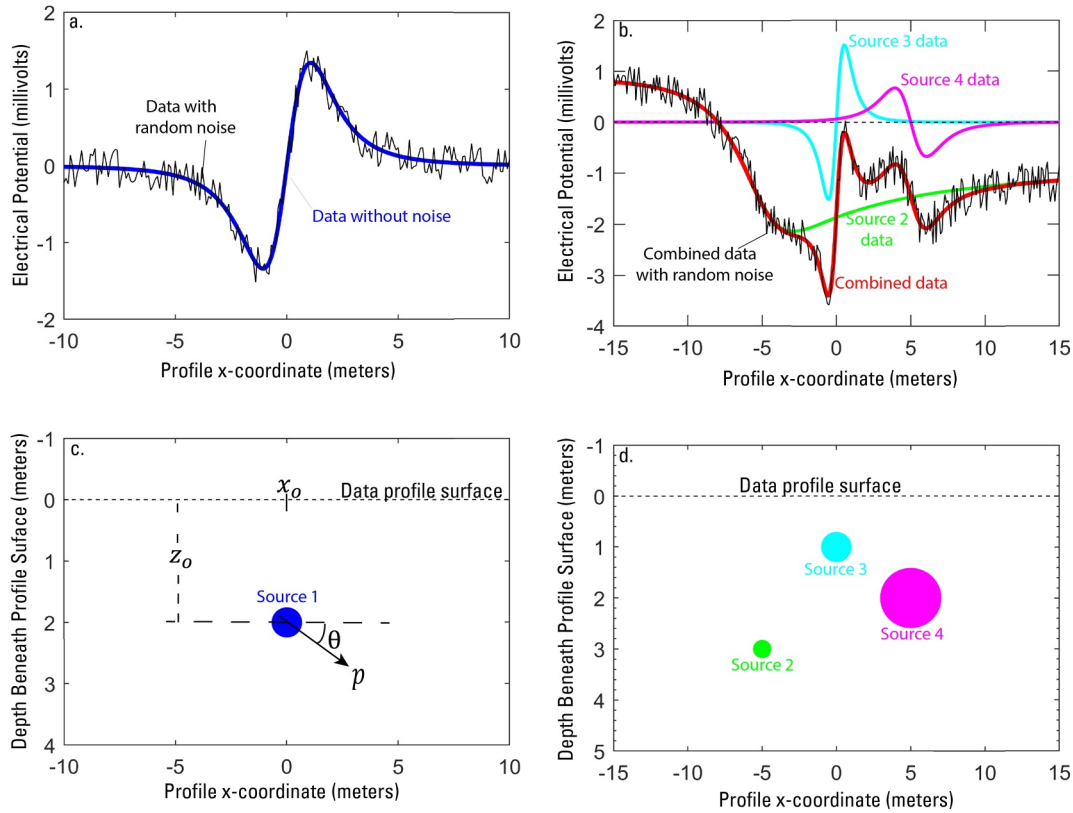

Figure 1. Conceptual models of buried electrically polarized sources of electrical potential and Equation 5-simulated synthetic electrical-potential profile data attributed to the electrical sources. (a) Horizontal electrical-potential profile data (dark blue) attributed to the dark-blue source shown in panel (c). (b) Horizontal electrical potential profiles attributed to three buried sources in panel (d). The red curve is the sum of the green, pink, and light-blue curves calculated from sources of corresponding color, and represents the horizontal electrical-potential profile data attributed to combined effect of the three sources. (c) Subsurface distribution of one electrical source that produces the true model (dark-blue data) in panel (a), showing Equation 5 parameters. (d) Subsurface distribution of three electrical sources that produce the true model (red data) in panel (b).

$$\varphi(x) = \sum_{i=1}^{m} p_i \frac{(x - x_o)\cos\theta_i + z_o \sin\theta_i}{\left[(x - x_o)^2 + z_o^2\right]^{q_i}} \tag{5}$$

In Equation 5, x_o (m) is the origin of the buried electrical source beneath the horizontal profile and z_o (m) is the depth to the center of the source in the case of spherical and horizontal cylindrical sources (Figure 1), or depth to the top of the source in the case of vertical cylindrical sources and inclined polarized sheet-like sources. The variable θ (radians) is the polarization angle between the axis of polarization of the source and the horizontal axis, and controls the symmetry of the electrical-potential anomaly along the profile around the x_o coordinate. The shape-factor, q (unitless), is typically assigned values of 1.5 for a spherical source, 1.0 for a horizontal cylindrical source, 0.5 for a vertical cylindrical source (Di Maio et al., 2019), and its value approaches 0 for a polarized plane (Göktürkler & Balkaya, 2012). Note that the value of the shape factor parameter affects the units of the electric-current dipole moment, p ($\text{mV} \cdot \text{m}^{2q-1}$), which for horizontal cylindrical sources ($q = 1$) is related to the electrical source-current density (I, Amps) and the resistivity of the geologic material according to Equation 6.

$$p = \frac{\rho I}{2\pi} \tag{6}$$

The dipole moment of the source is a vector quantity that represents the separation of positive and negative electrical charge. The vector direction points from the negative charge to the positive charge, and its magnitude

quantifies the intensity of the electric dipole (Biswas and Sharma, 2014a, 2014b). Advective separation of charge is an electrical-current source (Revil and Leroy, 2001), such that advective drag of excess electrical charge in the electrical double layer through the pore spaces of an aquifer by groundwater flow is expected to produce an electrical dipole-moment with a vector direction that reflects the groundwater-flow direction.

3. The Self-Potential Inverse Problem

The SP inverse problem presented in this work combines stochastic electrical-source localization using PSO and electrical-source tomography using weighted least-squares (WLS) minimization of a regularized quadratic objective function of weighted data residuals and weighted model vector. The analytical forward model of Equation 5 is used to circumvent the need for computationally expensive numerical solutions of the governing partial differential equations (Equations 1 and 2) and to precondition the kernel matrix of the WLS objective with prior information from stochastic source localization using PSO. The mechanics of the inversion procedure are summarized in the flow chart provided in the Supporting Information S1, which indicates the connection between the source-localization and source-tomography algorithms used in this work.

3.1. Source Localization by Particle Swarm Optimization

Source-localization optimizes the geospatial locations and electrical properties of an arbitrary number of stochastic electrical-current sources to minimize misfit between measured data and data simulated by the analytical forward model in Equation 5. The sources are considered stochastic in the sense that each is randomly positioned and assigned electrical properties by PSO to minimize the residual error (data misfit) between the measured data and the cumulative sum of simulated data attributed to all optimized stochastic sources. Equation 7 expresses the root mean squared error (RMSE) objective function to be minimized. In Equation 7, the $N\ x\ 1$ column vector $\mathbf{e} = \mathbf{d}_{\text{obs}} - \mathbf{d}_{\text{sim}}$ is the residual error vector, where N refers to the number of observed and simulated data and the superscript T denotes the vector and matrix transpose operator. The residual error vector is equal to the difference between observed (measured or analytical-model) electrical-potential data stored in the column vector, $\mathbf{d}_{\text{obs}}$, and simulated electrical-potential data stored in the column vector $\mathbf{d}_{\text{sim}}$ and simulated by substitution of the optimized source-parameters values into Equation 5.

$$\text{RMSE} = \left[\frac{1}{N}\mathbf{e}^{\text{T}}\mathbf{e}\right]^{1/2} \tag{7}$$

The PSO source-localization algorithm incorporates the following steps for each stochastic electrical source that it optimizes (Eberhart & Kennedy, 1995; Pekşen et al., 2011). A particle swarm is completed for each stochastic source. Each swarm consists of 2,000 particles initialized by random initial position and velocity vectors and local- and global-best position vectors with lengths equal to the number of parameters to be optimized (five parameters in Equation 5; p, θ, q, x_o, z_o). Equation 5 is evaluated for each particle to simulate electrical-potential data along the $z = 0$ surface. Equation 7 is evaluated for each particle to quantify the RMSE between measured and simulated data. The best positions of individual particles and the best global position of all particles in the swarm, as indicated by the lowest respective values of RMSE, are determined from Equation 7 and the local- and global-best position vectors are updated accordingly. The particles' positions and velocity vectors are then updated as shown in Equations 8 and 9 (Fernández-Martínez et al., 2010; Yuan et al., 2009).

$$\mathbf{v}_{\text{i}}^{\text{j}+1} = \text{w}\mathbf{v}_{\text{i}}^{\text{j}} + \text{c}_1\text{r}_1\left(\mathbf{p}_{\text{i}} - \mathbf{x}_{\text{i}}^{\text{j}}\right) + \text{c}_2\text{r}_2\left(\mathbf{g} - \mathbf{x}_{\text{i}}^{\text{j}}\right)\ i = 1\ldots s,\ j = 1,\ldots maxits \tag{8}$$

$$\mathbf{x}_{\text{i}}^{\text{j}+1} = \mathbf{x}_{\text{i}}^{\text{j}} + \mathbf{v}_{\text{i}}^{\text{j}+1} \tag{9}$$

In Equations 8 and 9, $i = 1, 2, \ldots, s$ is a particle index for each of the $s = 2{,}000$ particles in each swarm, the velocity vectors $\mathbf{v}_{\text{i}}^{\text{j}}$ and $\mathbf{v}_{\text{i}}^{\text{j}+1}$ are row vectors that represent the velocities of each of the particles at the jth and $(\text{j} + 1)^{\text{th}}$ iterations of the PSO algorithm to provide the parameter perturbations needed for iterative updating of the particle-position vectors. The row-vectors $\mathbf{x}_{\text{i}}^{\text{j}}$, $\mathbf{p}_{\text{i}}$, and $\mathbf{g}$ are, respectively, the position vector of the ith particle at iteration j, the best position vector of the ith individual particle out of all iterations, and the global best position vector from the entire swarm of particles out of all iterations. The maximum number of iterations (*maxits*) is

specified to balance accurately simulated electrical-potential profile data with computational speed. The position vector of a given particle is the set of parameter values corresponding to the particle at each iteration of the algorithm and represents an attempt to solve the inverse problem, whereas the global best position of the group of particles represents the best solution to the inverse problem that the algorithm converges upon for each stochastic electrical source that is optimized. The inertia weight, w (dimensionless), in Equations 8 and 9 is applied to each particle in a given swarm and specified as a decay function of the iteration number within the range [0.8, 1.2] (Essa, 2019; Monteiro Santos, 2010; Shi and Eberhart, 1998). Parameters c_1 and c_2 were each assigned a value of 2, whereas r_1 and r_2 were assigned uniformly distributed random numbers in the range [0, 1].

Stochastic sources are localized by the PSO algorithm consecutively one-by-one. PSO iteration occurs for each stochastic source until predefined convergence criteria are met. Upon each convergence for each stochastic source, the vectors $\mathbf{d}_{obs}$ and $\mathbf{d}_{sim}$ in Equation 7 are modified. Simulated data in $\mathbf{d}_{sim}$ are accumulated from prior stochastic sources according to Equation 10, where index S is the predefined maximum number of stochastic sources to be optimized, and the accumulated sum of simulated data is subtracted from $\mathbf{d}_{obs}$ according to Equation 11. This essentially modifies Equation 7 upon optimization of each stochastic source by consecutively decomposing $\mathbf{d}_{obs}$ and removing the contributions of optimized sources at prior iterations in accordance with the principle of superposition (Blakely, 1995; Griffiths, 1999). Thus, the algorithm localizes a specified number of sources one source at a time, and progressively minimizes the RMSE between measured data and the cumulative sum of simulated data for each stochastic source.

$$\mathbf{d}_{sim,S} = \sum_{j=1}^{S} \mathbf{d}_{sim,j} \tag{10}$$

$$\mathbf{d}_{obs} = \mathbf{d}_{obs} - \mathbf{d}_{sim,S} \tag{11}$$

3.2. Self-Potential Source Tomography by Weighted Least Squares

SP-source tomography images the spatial distribution of electrical-current sources beneath the horizontal profile of SP data on the $z = 0$ surface. The subsurface is discretized horizontally and vertically into $M = nx \cdot nz$ grid points, where nx is the number of discretized points in the horizontal x-coordinate direction and nz is the number of discretized points in the vertical z-coordinate direction. Each of the M discretized grid points beneath the horizontal profile is assumed to represent the fixed location of an electrical-current source, and the unknown values of dipole moments at each discretized point are optimized by minimizing an objective function of the weighted data-vector and model-vector norms shown in Equation 12, where $\|\mathbf{A}\|_2$ represents the L_2 Euclidean norm of an arbitrary vector $\mathbf{A}$ (Menke, 1989).

$$\min \|\mathbf{W_d}(\mathbf{d}_{sim} - \mathbf{d}_{obs})\|_2 + \lambda \|\mathbf{W_m}(\mathbf{m} - \mathbf{m_0})\|_2 \tag{12}$$

In Equation 12, $\mathbf{d}_{sim} = \mathbf{Km} = [d_{sim,1}, d_{sim,2}, \ldots d_{sim,N}]^T$, is an $N\,x\,1$ column-vector containing simulated electrical-potential data at the geospatial locations of each measured data. The measured data are stored in the $N\,x\,1$ column-vector $\mathbf{d}_{obs} = [d_1, d_2, \ldots d_N]^T$, and the residual error vector of residual errors between simulated and measured electrical-potential data, $\mathbf{e}$ (mV), is again defined as $\mathbf{e} = \mathbf{d}_{sim} - \mathbf{d}_{obs}$. The matrix $\mathbf{K}$ is an $N\,x\,M$ forward-model kernel matrix that encodes the physics of the forward problem in addition to the horizontal and vertical discretization intervals. The values of dipole-moments of the electrical sources at the discretized grid points are stored in the $M\,x\,1$ model vector $\mathbf{m} = [p_1, p_2, \ldots p_M]^T$, and their optimized values approximate the N measured data to an acceptable degree from the analytical forward model. The matrices $\mathbf{W_d}$ and $\mathbf{W_m}$ in Equation 12 are data-weighting and model-weighting matrices, respectively, that enable prior information to be incorporated into the algorithm. The dimensionless parameter λ is a scalar regularization parameter that optimizes a trade-off between residual error and model complexity and enables a unique inversion model to be determined without overfitting noise in the observed data (Aster et al., 2005; Tikhonov and Arsenin, 1977). The $M\,x\,1$ column-vector $\mathbf{m}_0$ represents a reference model and in this work was equal to the zero vector.

Minimization of the objective function in Equation 12 leads to the linear system of equations expressed in Equation 13. Equation 13 is solved by restating it as an $N\,x\,M$ linear system of equations $\mathbf{Gm} = \mathbf{d}^*$, where $\mathbf{G}$ is an $N\,x\,M$ matrix that represents the bracketed term on the left-hand side of Equation 13 and $\mathbf{d}^*$ is an $N\,x\,1$ column

vector that represents the bracketed term on the right-hand side. The inverse model corresponding to a single value of λ is then obtained by truncated singular-value decomposition of $\mathbf{G}$ into $\mathbf{G} = \mathbf{U}\Sigma\mathbf{V}^{\mathrm{T}}$, where $\mathbf{U}$ is an $M\ x\ M$ orthogonal matrix of basis vectors spanning the data space, Σ is an $M\ x\ N$ diagonal matrix with singular values of $\mathbf{G}$ on the diagonal, and $\mathbf{V}$ is an $N\ x\ N$ orthogonal matrix with basis vectors spanning the model space (Aster et al., 2005). The solution of Equation 13 is obtained from Equation 14, where Σ_j is the jth singular value of the matrix $\mathbf{G}$, $\mathbf{U}_{\mathrm{j}}^{\mathrm{T}}$ is the transposed jth column of matrix $\mathbf{U}$, and $\mathbf{V}_{\mathrm{j}}$ represents the jth column of the matrix $\mathbf{V}$ (Aster et al., 2005).

$$\left[\mathbf{K}^{\mathrm{T}}\left(\mathbf{W}_{\mathrm{d}}^{\mathrm{T}}\mathbf{W}_{\mathrm{d}}\mathbf{K}\right) + \lambda\left(\mathbf{W}_{\mathrm{m}}^{\mathrm{T}}\mathbf{W}_{\mathrm{m}}\right)\right]\mathbf{m} = \left[\mathbf{K}^{\mathrm{T}}\left(\mathbf{W}_{\mathrm{d}}^{\mathrm{T}}\mathbf{W}_{\mathrm{d}}\right)\mathbf{d}_{\mathrm{obs}} + \lambda\left(\mathbf{W}_{\mathrm{m}}^{\mathrm{T}}\mathbf{W}_{\mathrm{m}}\right)\mathbf{m}_{o}\right] \tag{13}$$

$$\mathbf{m} = \sum_{\mathrm{j=1}}^{\mathrm{min(M,N)}} \frac{\Sigma_{\mathrm{j}}^{2}}{\Sigma_{\mathrm{j}}^{2} + \lambda^{2}} \frac{\mathbf{U}_{\mathrm{j}}^{\mathrm{T}}\mathbf{d}}{\Sigma_{\mathrm{j}}}\mathbf{V}_{\mathrm{j}} \tag{14}$$

Data and model weighting matrices are incorporated into Equation 13 to add prior information regarding data quality, model discretization intervals, and model smoothness (Aster et al., 2005; Menke, 1989). The data-weighting matrix, $\mathbf{W}_{\mathrm{d}}$, is the $N\ x\ N$ diagonal matrix defined in Equation 15 that contains along its diagonal the reciprocals of standard deviations σ_n of data measured over a window of values preceding and following each of the measured values in $\mathbf{d}_{\mathrm{obs}}$. Larger weighting represents electrical-potential data that are characterized by smaller standard deviation, and vice versa.

$$\mathbf{W}_{\mathbf{d}} = \mathrm{diag}\left[{}^{1}\!/_{\sigma_1}, \ldots, {}^{1}\!/_{\sigma_N}\right] \quad j = 1, \ldots, N \tag{15}$$

The model weighting-matrix, $\mathbf{W}_{\mathbf{m}}$, is an $M\ x\ M$ matrix that affects properties of the inverse solution such as depth-weighting of the inverted sources, model-smoothness and source-compactness constraints in the x and z coordinate directions. The inversion algorithm developed in this work enables calculation of the model-weighting matrix by two methods. In the primary method, $\mathbf{W}_{\mathrm{m}}$ is calculated as the discrete banded Laplacian matrix based on a modified form of the code published by LeVeque (2007, p. 68), and explicit calculation of the matrix $\mathbf{W}_{\mathbf{m}}^{\mathrm{T}}\mathbf{W}_{\mathbf{m}}$ is obtained from $\mathbf{W}_{\mathbf{m}}$. Alternatively, model-weighting is incorporated through linear subspace methods described by (Li & Oldenburg, 1996, 1998, 2000; Oldenburg and Li, 1994) to allow for inclusion of depth-weighting and additional prior information. These methods are described in further detail in the Supporting Information S1.

The kernel matrix $\mathbf{K}$ in Equation 13 is calculated from the forward model in Equation 5 in two steps. First, PSO is applied to Equation 5 to optimize a predefined number of stochastic electrical-current sources and minimize residuals between measured and simulated electrical-potential data. Second, a parametric sweep is performed over discretized model grid points. Each grid point is used in succession as an electrical-current-source boundary condition with fixed position and standardized electrical properties ($p = 1$ mV · m, $\theta = 0°$, $q = 1$), while the remaining model points are assigned dipole moments equal to 0 mV · m. Discretized model grid points located on or near a stochastic source are assigned the dipole moment of the stochastic source, whereas the polarization-angle and shape-factor parameters are held constant at the standardized values (to maintain proper units). Electrical-potential data along the $z = 0$ surface are calculated by using Equation 5 for each current-source at each grid point, and each vector of simulated profile data is stored in a matrix as a row vector. The parametric sweep over the full set of discretized model points produces the $M\ x\ N$ matrix $\mathbf{K}^{\mathrm{T}}$, which is transposed into the $N\ x\ M$ matrix $\mathbf{K}$ on the basis of source-receiver reciprocity and substituted into Equation 13. In this manner, the PSO step reduces noise in the electrical-potential data inverted by the source-tomography algorithm, and the optimized dipole-moment values of the stochastic sources precondition the tomography inverse problem with prior information about the locations and intensities of stochastic electrical current sources.

The SP inverse problem is underdetermined because there are more unknown parameters in $\mathbf{m}$ than there are synthetic (or measured) SP data in $\mathbf{d}_{\mathrm{obs}}$. An infinite number of inverse model vectors $\mathbf{m}$ can therefore reproduce the measured data exactly by fitting noise in the data. Regularization was therefore applied by solving Equation 13 30 separate times using logarithmically spaced values of λ within the interval $[10^{-5}, 10^{5}]$ to quantify the L_2 data-vector and L_2 model-vector norms corresponding to each unique value of the λ parameter (Aster et al., 2005;

Table 1
Summary of Equation 5 Parameter Values of Synthetic Model Sources Shown in Figure 1, With Comparison of Values Estimated by Particle Swarm Optimization of 1 and 3-Source Synthetic-Model Data by Percentage of Added Noise

			Simulated parameter values				[a]Relative error			
Equation 5 parameter	Synthetic source (Figure 1)	True parameter values	[b]0 Percent noise	[c]5 Percent noise	[d]10 Percent noise	[e]50 Percent noise	0 Percent noise	5 Percent noise	10 Percent noise	50 Percent noise
$\boldsymbol{p}$ (mV^{2q-1})	1	50	50.00	61.07	42.50	−9.92	0.00	22.14	−15.00	−119.84
	2	−3	−2.90	−2.92	−2.87	−2.74	−3.33	−2.74	−4.20	−8.63
	3	−25	−9.14	−4.80	−60.00	−17.02	−63.42	−80.80	139.99	−31.92
	4	5	3.71	3.57	4.26	−1.76	−25.71	−28.67	−14.84	−135.22
θ (radians)	1	0	0.00	3.15	0.00	3.20	[f]3.15	[f]0.00	[f]3.20	[f]3.15
	2	0.785	0.85	0.86	0.81	0.85	8.47	9.64	2.78	7.65
	3	0	0.09	0.12	0.08	0.07	[f]0.09	[f]0.12	[f]0.08	[f]0.07
	4	0	0.05	0.08	0.01	3.08	[f]0.05	[f]0.08	[f]0.01	[f]3.08
z_o(m)	1	2	2.00	2.09	1.98	1.46	0.00	4.50	−1.00	−27.00
	2	3	2.60	2.55	2.87	2.61	−13.24	−15.02	−4.28	−13.00
	3	2	1.69	1.45	2.17	1.65	−15.63	−27.59	8.67	−17.41
	4	1	0.93	0.92	0.96	0.70	−6.96	−8.33	−3.99	−30.10
q (unitless)	1	2.25	2.25	2.28	2.17	1.77	0.00	1.33	−3.56	−21.33
	2	0.625	0.61	0.61	0.62	0.61	−1.98	−2.32	−1.35	−2.94
	3	2.25	1.96	1.75	2.57	2.01	−12.73	−22.22	14.41	−10.76
	4	2.25	1.95	1.92	1.96	2.26	−13.44	−14.69	−12.95	0.28
x_o(m)	1	[g]0	–	–	–	–	–	–	–	–
	2	−5	−4.87	−4.82	−5.09	−4.59	−2.60	−3.58	1.88	−8.18
	3	5	5.13	5.18	5.25	5.09	2.70	3.57	5.01	1.87
	4	0	0.05	0.08	−0.02	0.03	[f]0.05	[f]0.08	[f]−0.02	[f]0.03

Note. All simulations were performed with specified criteria of 2,000 particles, 60 maximum iterations before convergence is assumed, and root mean square error (RMSE) of convergence equal to 0.0001 mV. [a]Relative error (RE) is calculated as RE = 100 · (simulatedvalue-truevalue)/truevalue. [b]Root mean square error between the simulated electrical-potential data for the optimized parameter set and the electrical-potential data corresponding to the true parameter values equal to 0.0259 mV. [c]Root mean square error between the simulated electrical-potential data for the optimized parameter set and the electrical-potential data corresponding to the true parameter values equal to 0.0324 mV. [d]Root mean square error between the simulated electrical-potential data for the optimized parameter set and the electrical-potential data corresponding to the true parameter values equal to 0.0251 mV. [e]Root mean square error between the simulated electrical-potential data for the optimized parameter set and the electrical-potential data corresponding to the true parameter values equal to 0.0879 mV. [f]Absolute difference computed because the true parameter value = 0. [g]The x_o parameter was fixed and not an optimized parameter for the 1-source synthetic model.

Hansen & O'Leary, 1993; Oliveti and Cardarelli, 2019; Tikhonov and Arsenin, 1977). The procedure for automated selection of the regularization parameter is described in further detail in the Supporting Information S1.

4. Application to Synthetic Model Data

The source-localization and source-tomography algorithms outlined in Section 3 are tested in this section on synthetic models of electrical-current sources characterized by simple geometric shapes to evaluate the performance of the algorithms for varying percentages of electrical noise in the inverted data. Figures 1a and 1b show synthetic electrical-potential profiles calculated with Equation 5 and attributed to synthetic electrical sources in Figures 1c and 1d whose diameters are sized proportional to the assigned dipole moments of the sources, which are summarized in Table 1. The shape factors (q values in Table 1) of the synthetic sources shown in Figure 1 most closely resemble spherical and vertical-cylindrical sources based on their values. Figure 1a shows synthetic electrical-potential data attributed to the single buried source positioned at the location of the dark-blue circle in Figure 1c. The dark-blue data in Figure 1a represents synthetic data without noise and the black data represents synthetic data contaminated with 10% Gaussian random noise. The percentage of added noise is relative to the amplitude of the synthetic anomaly, defined herein as the difference between the maximum and minimum values

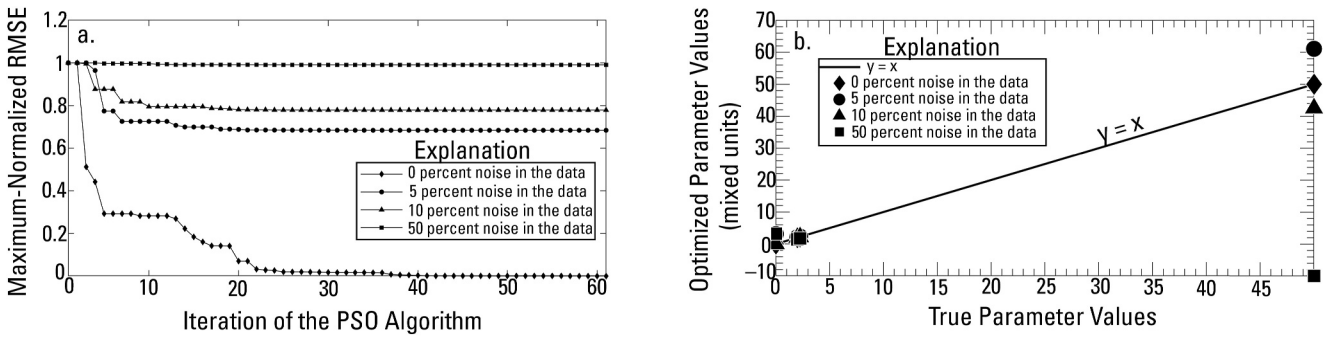

Figure 2. Comparison of convergence and simulated parameter values of the 1-source synthetic model for inversion of data with variable percentages of noise. (a) Convergence of the particle swarm optimization algorithm. (b) Comparison of true parameter values with optimized parameter values for the 1-source synthetic models with 0, 5, 10, and 50% added noise.

of the synthetic data. Figure 1b shows calculated electrical-potential data profiles whose colors correspond to the three sources in Figure 1d. The red data is the cumulative sum of the three individual data profiles and the black data equals the red data with the addition of 10% noise.

Figure 2 illustrates the convergence characteristics of the PSO source-localization algorithm applied to the 1-source synthetic model shown in Figures 1a and 1c. Figure 2a shows PSO algorithm convergence on the true source parameters corresponding to the noise-free (blue) and noisy (black) data in Figure 1a. In each case, PSO iteration repeated until pre-defined convergence criteria were met; either the maximum number of 60 allowed iterations was exceeded or the RMSE between simulated and noisy synthetic-model electrical-potential data was less than 0.0001 mV. Figure 2b shows a scatter plot of true versus simulated parameter values for application of the PSO algorithm to the noise-free data and noisy synthetic model data corresponding to the 1-source model in Figure 1c. The PSO algorithm converges within 10–35 iterations for both noise-free and noisy synthetic-model data containing as much as 10% noise, and recovers the parameters of the 1-source synthetic model accurately for the noise-free data and the data contaminated with 5% and 10% noise. The inverted parameters resulted in RMSE between simulated horizontal electrical potential profile data and true data from true parameter values equal to 0.0 mV, 0.00537 mV, 0.00372 mV, 0.02737 mV, respectively, for inversion of data with 0, 5, 10, and 50% noise.

Figure 3 demonstrates source localization by PSO on the 3-source synthetic model in Figure 1d. Additionally, Figure 3 illustrates the process of modifying the objective function by Equations 10 and 11 during PSO of each of the three synthetic sources shown in Figure 1d. The process is depicted for inversion of both the noise-free (red) and noisy (black) electrical-potential profile data shown in Figure 1b. Figures 3a–3f show PSO applied to the noise-free data, whereas Figures 3g–3l show PSO optimization of noisy data for 5, 10, and 50% noise added to the data. Figures 3d–3f show the progressive optimization of each of the three synthetic electrical sources by the black asterisks adjacent to the pink, light-blue, and green synthetic sources. The dark-blue data in Figures 3a–3c represent the simulated data after optimizing the positions and electrical parameters of stochastic sources represented by the black asterisks in Figures 3d–3f. The sources are not optimized in any particular order because they are stochastic. In Figure 3a, the green source was optimized first by the PSO algorithm and the optimized source parameters were substituted into Equation 5 to simulate the dark-blue electrical-potential data in Figure 3a, which approximates the synthetic data attributed to the green source. The dark-blue data in Figure 3a were subtracted from the red curve, and added to the simulated data curve from the previous source (which in the case of optimizing the first stochastic source was the zero vector) according to Equations 10 and 11. The second stochastic source was added to the subsurface by the PSO algorithm and its position and electrical properties were optimized to minimize residual error between the cumulative simulated data and the modified objective function. The cumulative effect is shown in Figure 3b by the dark-blue curve that approximates the part of the green curve and one of the two relative positive peaks of the noise-free cumulative anomaly (the peak attributed to the presence of the light-blue source). Equations 10 and 11 were applied again, and the third stochastic electrical source was added and optimized by the PSO algorithm to approximate the properties of the pink source and ultimately reproduce the red curve in Figure 3c from the combination of sources. The same process was applied to the black curves in Figures 3g–3l to demonstrate the robust nature of the PSO algorithm for finding electrical sources by inversion of data contaminated by adding varying amounts of noise ranging from 0 to as much as 50%.

10.1029/2024WR037549

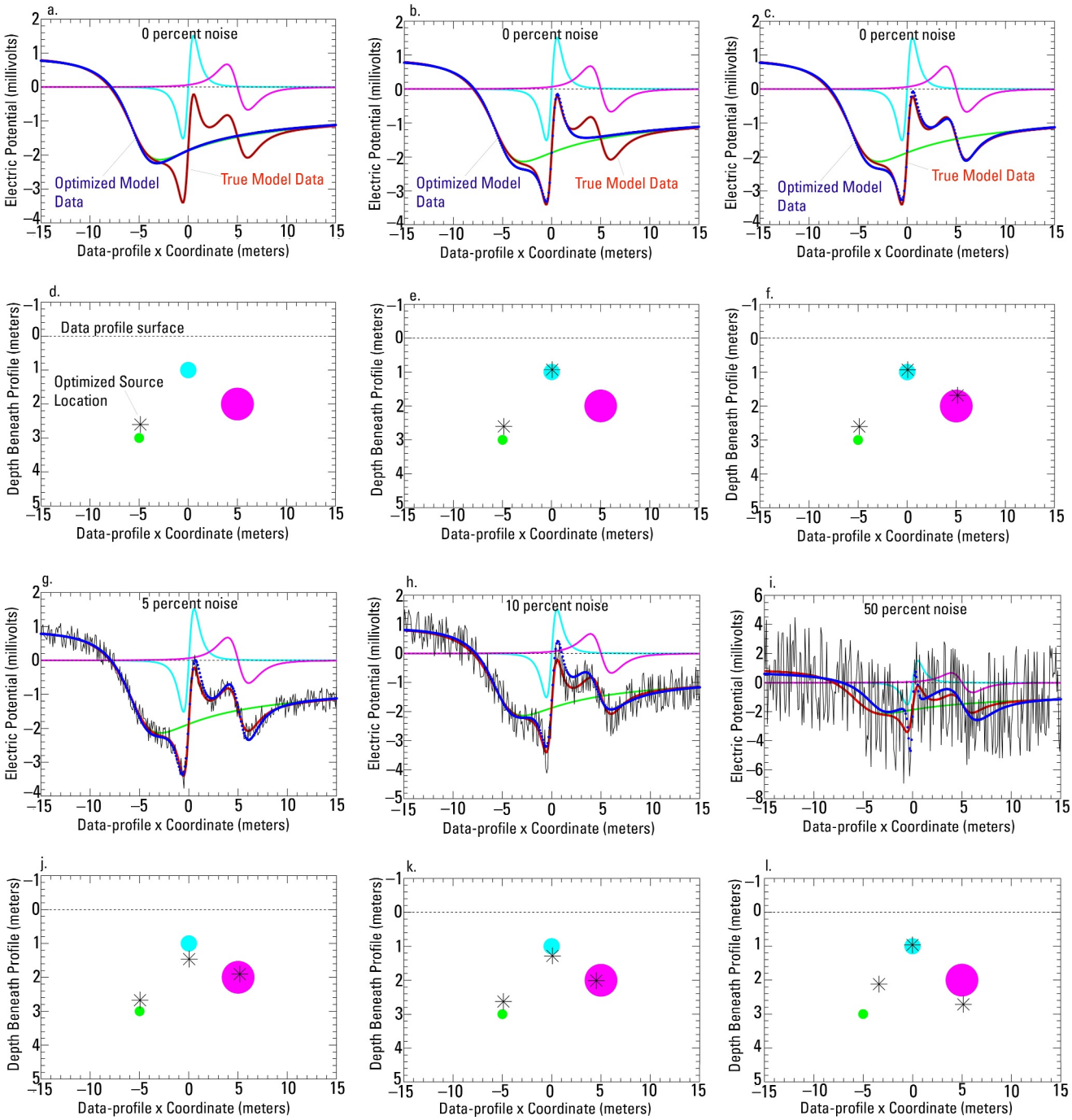

Figure 3. Illustration of the progression of particle swarm optimization (PSO) of Equation 5 parameters of synthetic electrical sources with and without Gaussian random noise added to the synthetic data. (a–c) Electrical-potential profiles calculated with Equation 5 attributed to electrical-current sources with simplified geometry, with composite electrical-potential anomaly (red curve) simulated from the three individual sources in panels (d–f), whose corresponding electrical-potential profile data are shown by the blue, pink, and green curves. The dark blue curves show the progression PSO of each electrical source. (d–f) Subsurface distribution of electrical sources that produce the true model (red) and noisy true model (black) in panels (a–f). (g–i) Inversions of synthetic electrical potential data with varying degrees of noise shown by the black curves. (j–l) Source distributions determined by PSO applied to noisy data in panels (h–j). In panels (d–f) and (j–l), colored circles represent the true locations of the synthetic sources whereas the asterisks represent the locations of sources estimated by PSO.

The PSO algorithm shows good accuracy with respect to identifying the locations of the pink and blue sources (see Figure 3l) and fair accuracy for identifying the location of the green source considering the data are contaminated with 50% noise and the green source is the weakest of the three synthetic sources.

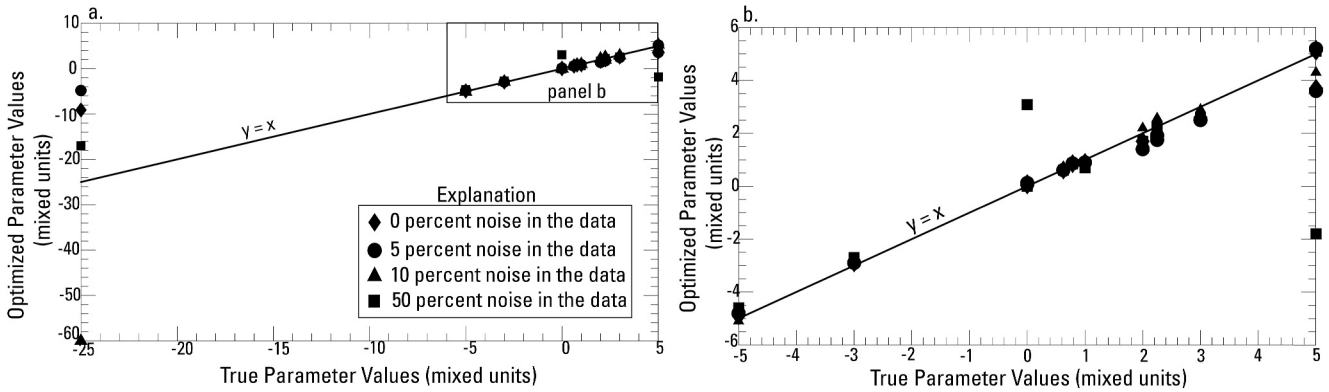

Figure 4. Comparison of true versus simulated synthetic-model parameters for optimizations of the 3-source synthetic models depicted in Figure 3 for differing percentages of noise added to the true synthetic-model data. (a) Full comparison for all parameters. (b) Enlarged view of parameter comparisons within the black rectangle in panel (a).

Figure 4 compares true and optimized parameter values of the 3-source synthetic models for the different percentages of noise added to the synthetic-model data. Figure 4b shows an enlarged region of Figure 4a. The comparison indicates the optimized parameters of the stochastic sources represented by black asterisks in Figures 3j–3l approximated the true parameter values by clustering around the line $y = x$ for all percentages of added noise, with the exception of the dipole-moments of the light-blue and pink sources (sources 3–4, Table 1) in the presence of excessive noise in the data (greater than 10%).

Figure 5 shows results of the WLS source-tomography algorithm applied to the 3-source synthetic model. The columns of Figure 5 represent inversions with increasing percentages of noise added to the synthetic-model data, for cases of 0, 10, and 50% added noise. The rows of Figure 5 represent inversions of data by the WLS algorithm with varied preconditioning applied to the objective function by PSO. Figure 5a shows a reference case where noisy-synthetic model data are inverted by the WLS algorithm without any applied preconditioning. Figures 5b and 5c show cases with variable preconditioning by PSO applied. Preconditioning, when applied, is applied either

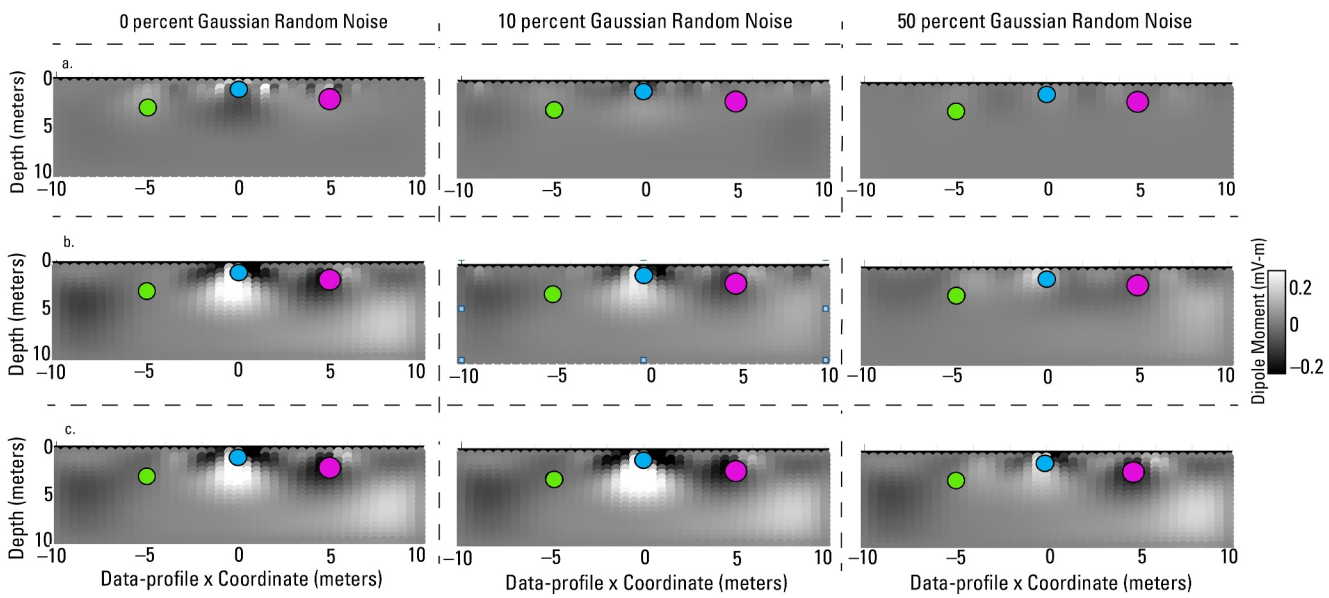

Figure 5. Illustration of source tomography of 3-source synthetic model data with varied percentages of added noise with and without preconditioning the kernel matrix of the weighted least-squares (WLS) objective function by particle swarm optimization (PSO). Columns represent varied percentages of added noise and rows represent varied precondition of the objective function. (a) Inversion of noisy synthetic model data by WLS without preconditioning by PSO-simulated data or sources. (b) Inversion of noisy synthetic model data by WLS by preconditioning the objective function with stochastic sources determined by PSO. (c) Inversion of the PSO-simulated data by WLS with stochastic sources used to precondition the objective function.

(a) by inverting noisy synthetic-model data with stochastic sources distributed into the kernel matrix of the objective function (Figure 5b) or (b) by inverting PSO simulated data with stochastic sources distributed into the kernel matrix (Figure 5c). The effect of inverting PSO simulated data as opposed to noisy synthetic-model data is a substantial reduction in the data noise imparted into the inverse-model solution. This is evident in Figure 3, where the PSO-simulated data shown by the blue data approximates the true model data shown by the red data well for all percentages of added noise. In Figure 5, the effect of preconditioning the kernel matrix with stochastic sources from PSO is an enhanced elucidation of the blue and pink synthetic sources for all percentages of added noise.

5. Monitoring Hyporheic Exchange in a Bedrock River

In the related work by Ikard et al. (2023b), two hydrologically active faults were identified by geoelectric surveys at a study site at East Fork Poplar Creek (East Fork) in Oak Ridge, Tennessee. The faults are depicted in electrical resistivity data in Figures 6 and 7 and labeled the north and south faults. In this current work, the north fault was targeted for SP monitoring, and the inversion algorithms described in Sections 3 were applied to SP-monitoring data measured on the East Fork flood plain about 2–3 m offset from the streambank to investigate hyporheic exchange occurring between the stream and the bedrock aquifer.

5.1. Description of the Study Area

The study site is shown in Figure 6. Figure 6a shows the regional setting of the study site and shows the location of the monitoring site relative to streamflow gage EFK5.4 operated by Oak Ridge National Laboratory and the study site of Rucker et al. (2021) approximately 310 m upstream from the SP monitoring site. Figure 6b shows a photograph of the western flood plain taken from the eastern flood plain during installation of the SP monitoring instrumentation. The general geophysical survey layouts at the study site are shown in Figure 6c relative to the Ikard et al. (2023b) WaSP and electrical resistivity tomography (ERT) data acquisition and the East Fork stream. Figure 6d shows an annotated photograph of the study area taken a few meters upstream from the parallel SP monitoring array looking downstream. The annotated photograph shows the general locations of the installed monitoring instrumentation and the prior data collection, and provides a good indicator of some salient hydrogeological characteristics of the site including the dense vegetation, stream channel geometry, and characteristics of the flood plain.

The hydrogeology of the survey area has been previously characterized by Rucker et al. (2021), Mohamed et al. (2021a, 2021b), Tsai et al. (2022), and Ikard et al. (2023b) and is summarized here from these sources. The resistivity distribution beneath survey lines ERT0 and ERT1 (Figure 7) show structural features that were interpreted by Ikard et al. (2023b) as intersecting faults, but which may also be karst features and complex intertwined networks of bedrock fractures. These features in the ERT data align spatially with WaSP anomalies measured directly in the stream (Figure 7b), as well as with a fractured-bedrock outcrop on the western flood plain at the study site (see Figure 1 in Ikard et al. (2023b)). Hyporheic exchange between the stream and flood plain is thought to occur predominantly lateral to the stream through the porous flood plain sediments and vertically along fracture planes through the limestone bedrock outcrops and streambed (Mohamed et al., 2021a). For example, in 2012 water-level altitudes measured in flood plain piezometers installed along the EFK5.4 reach were higher than the altitude of the stream, such that the hydraulic head decreased from the flood plain toward the stream (Mohamed et al., 2021a; Rucker et al., 2021). This prior work measured gradients in the unconsolidated sediments under only baseflow conditions and showed groundwater discharge to the stream; however, gaining stream conditions may not occur everywhere, particularly where groundwater exchange is dominated by fracture and fault flow (Mohamed et al., 2021a). The WaSP anomaly measured at the north fault in January 2021 (Figure 7b) indicated a possible vertical component surface-water loss occurred along faults and fracture planes that intersect the bedrock streambed.

Two SP monitoring arrays were installed into the East Fork flood plain near the north fault in March 2023. Each consisted of multiple non-polarizing copper-sulfate electrodes that were connected to a multiplexor and datalogger. Both monitoring arrays used a common reference electrode, which was buried at the location of the datalogger and isolated from the arrays (see location in Figure 6c). The first array was 87-m long and consisted of 30 electrodes buried in a trench on the east flood plain parallel to the streambed and offset by 2–3 m from the edge of the bank (see Figure 6b), with each electrode separated from adjacent electrodes by a 3-m interval. This array,

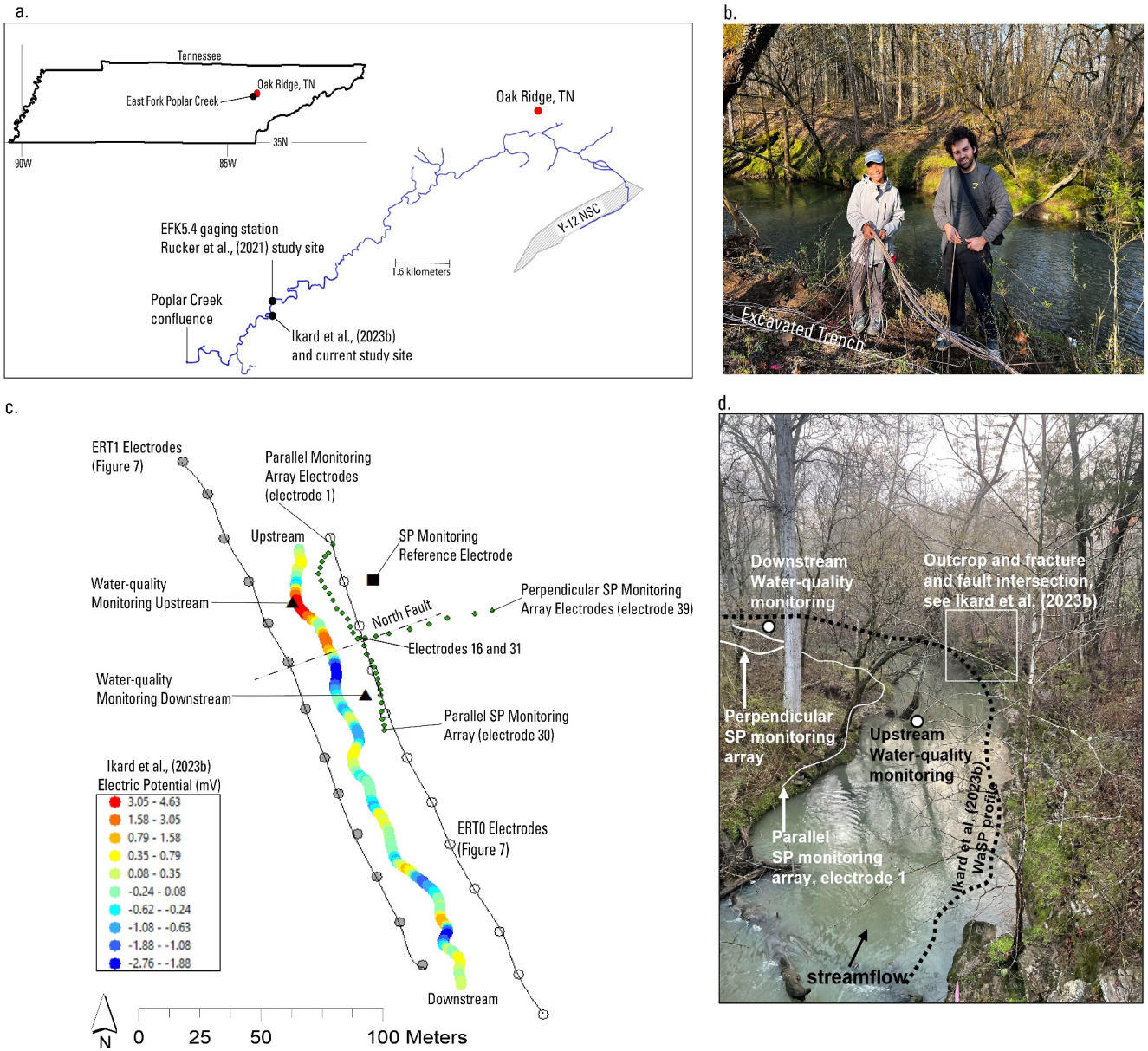

Figure 6. Location maps and photographs of the survey area of East Fork Poplar Creek. (a) Geographic and reach-scale location maps of the survey area. (b) Photograph on 23 March 2023, of New Mexico State University students installing the parallel monitoring array. (c) Map of the monitoring instrumentation installed into the flood plain and stream of East Fork Poplar Creek showing previous waterborne self-potential and electrical resistivity tomography survey lines. (d) Photograph on 23 March 2023, of the survey area annotated from the layout map in panel (c).

referred to herein as the "parallel" SP monitoring array, was positioned parallel with the stream between WaSP profile x-coordinates of 0 and 87 m (Figure 7b), and intersected the north fault transversely approximately at the array midpoint. The second array, referred to herein as the "perpendicular" array, was 40-m long and consisted of 9 electrodes laid out approximately perpendicular to the streambed and separated from one another by a 5-m interval. Electrodes of the perpendicular array were positioned to approximately coincide with the north fault. Figure 6b shows a photograph of installation of the parallel monitoring array. Electrodes were implanted 30–45 cm beneath the base of an excavated trench. Stranded copper wire (14 gauge) was connected to each electrode by waterproof terminal caps, bundled together with zip ties and run back through the trench to the reference electrode where they were wired into the data logger. The datalogger was programmed to make differential measurements between every electrode and the reference electrode every 60 s between 16:13:00 Eastern Standard Time (EST) on 26 March 2023, and 11:41:00 EST on 14 September 2023.

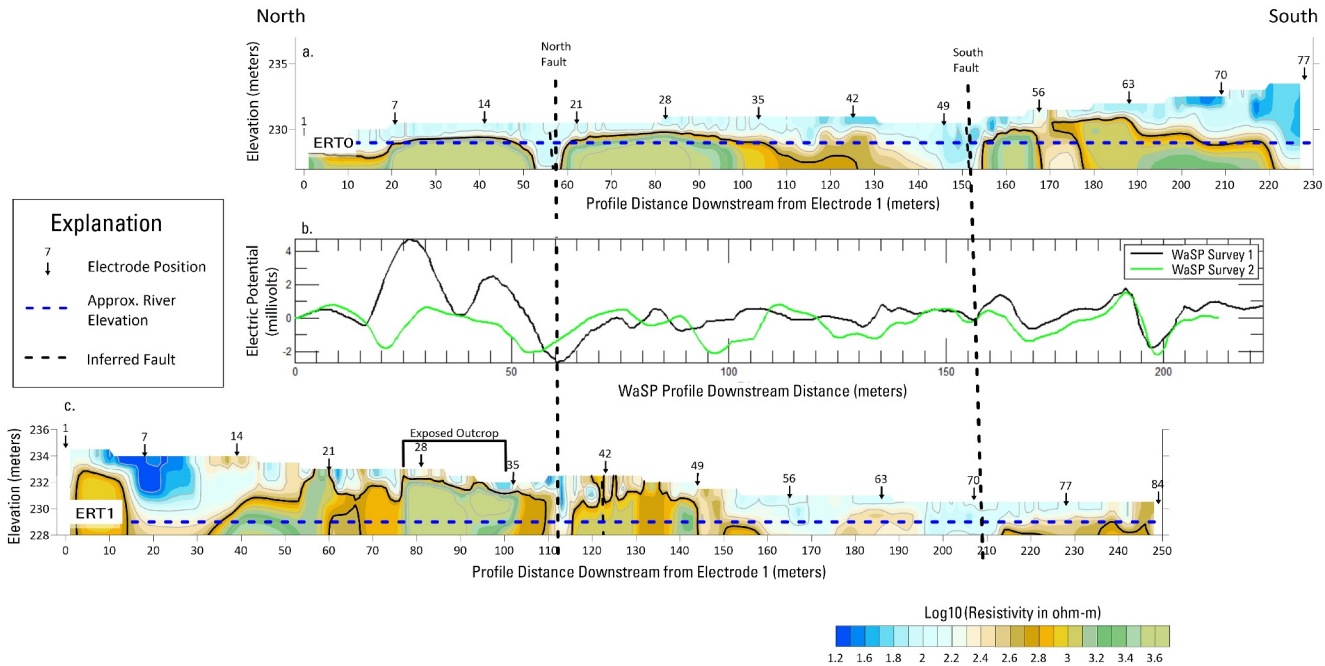

Figure 7. Comparison of electric resistivity tomography (ERT) survey data and electrical-potential profile data along coincident waterborne self-potential (WaSP) profiles 1–2. (a) ERT survey line ERT0 located on the east flood plain of East Fork Poplar Creek. (b) WaSP profile data measured in the stream along the west bank of East Fork Poplar Creek. (c) ERT survey line ERT1 located on the west flood plain of East Fork Poplar Creek. The black contour in the ERT data delineates the bedrock surface interpreted from the resistivity distribution.

Figure 8 shows raw voltage-difference measurements (black data) measured every 60 s at one selected electrode in the parallel monitoring array for approximately 157 days. Additional data from selected electrodes upstream and downstream from, and on top of the north fault are provided in the Supporting Information S1. Data processing steps are summarized in a flow chart in the Supporting Information S1 and depicted in Figure 8a for a general consideration of their relevance to the inverted data and the inversion results. The processed time series of measured voltage-differences at each electrode of the parallel monitoring array are shown in Figure 8b, which depicts the collection of processed data by every electrode, as represented by the red curve in Figure 8a for processed data from one single electrode. The colors of each time-series indicates the spatial position of the corresponding measurement electrode within the monitoring array, with the cooler colors (blues, greens) representing electrodes at the upstream end of the parallel monitoring array (upstream from the north fault) and the warmer colored time-series (yellow, orange, red) corresponding to electrodes progressively further downstream along the array. The corresponding time-series of electrical-potential at each electrode in the parallel array are shown in Figure 8c, and a single instance of electrical-potential profile data along the parallel monitoring array is shown in Figure 8d corresponding to the measurement time indicated by the vertical black bar in Figures 8b and 8c. Each measurement time in Figure 8c represents a single spatial profile of electrical potential along the parallel monitoring array, and each spatial profile of electrical potential was inverted as described in Section 3 to image the subsurface distribution of electrical-current sources through time.

5.2. Inversion of the Self-Potential Monitoring Data

The parallel and perpendicular monitoring array profiles were discretized horizontally and vertically every 0.5 m to a depth of $z = 10$ m. This discretization resulted in 3,500 discretized points beneath the parallel monitoring array and 1,620 discretized points beneath the perpendicular monitoring array. The diagonal of the data weighting matrix was calculated for each inversion by applying a windowed standard deviation filter (window width = 7 samples) to the electrical potential profile data measured along each monitoring array. The discrete banded Laplacian matrix was used as the model weighting matrix for each inversion of the SP monitoring data. Regularization was performed every 60 inversions, which corresponded to one regularization for every hour of monitoring time. An automated methodology was implemented for selecting the regularized inverse model from

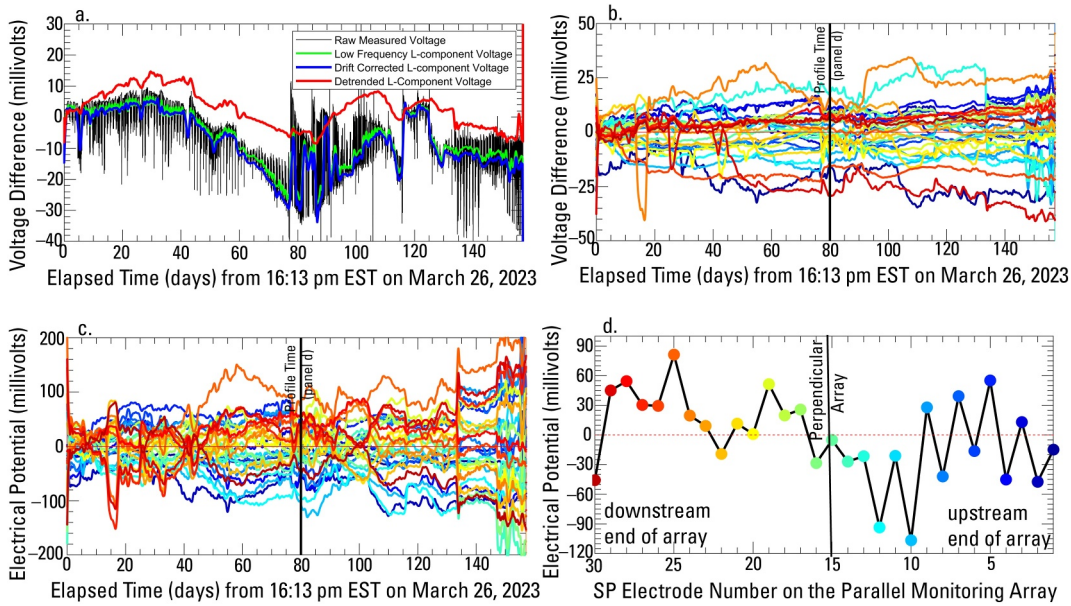

Figure 8. Time-series and spatial self-potential (SP) monitoring data measured on the parallel monitoring array, with an illustration of the data-processing steps completed prior to inversion. (a) Raw SP data (black data) measured on a single electrode upstream from the north fault with intermediate results of data-processing steps. The green data shows the low frequency variation of the raw data. The blue data shows the result of applying transient electrode-drift corrections to the green data. The red data shows the result of applying a linear spatial-trend correction and notch-filtering to the blue data. (b) The collection of processed time-series data analogous to the red data in panel (a), albeit for every electrode in the parallel monitoring array. Colors are varied to represent the electrode number shown in panel (d). (c) The time-series of electrical potential produced by numerical integration of the time-series data shown in panel (b). (d) Spatial profile of processed electrical-potential data along the parallel monitoring array at a single measurement time indicated by the vertical black lines in panels (b–c). The vertical black line in (d) shows the intersection point of the perpendicular and parallel monitoring arrays.

the regularization data. This methodology is depicted in the Supporting Information S1 for one single inversion, and the full time-series of automatically selected values of the regularization parameter are shown in the Supporting Information S1 for the parallel and perpendicular monitoring arrays.

Figure 9 depicts the spatial distribution of stochastic electrical sources beneath the monitoring arrays that were accumulated through time by PSO applied to the measured electrical-potential profile data. The distribution of dipole moments of the stochastic sources beneath the parallel monitoring array are depicted in Figure 9a, whereas the shape-factor and polarization-angle parameters of the sources, respectively, beneath the parallel monitoring array are depicted in Figures 9b and 9c. Figure 9d plots the dipole moment of the stochastic sources beneath the perpendicular monitoring array. The full collection of stochastic sources shown in Figure 9 illustrates how the subsurface electrical layering differs between the parallel and perpendicular monitoring arrays.

Figure 10 shows an SP tomogram produced by inversion of one time-lapse profile of electrical-potential data across each monitoring array. Figure 10a corresponds to the parallel monitoring array and compares measured electrical-potential data (black data) to simulated electrical-potential data representing source-localization by the PSO algorithm (green data) and source tomography by the WLS algorithm (pink data). The $x = 0$ coordinates correspond to SP electrode 1 at the upstream end of the electrode of the parallel array and electrode 31 closest to the stream on the perpendicular monitoring array. The simulated electrical-potential data produced by both the PSO and WLS algorithms approximates the measured data indicating that the regularized inverse model of spatial distribution of dipole-moments depicted in Figure 10b is a valid unique model. Figure 10b shows the distribution of inverted electric dipole moments beneath the parallel monitoring array corresponding to the electrical-potential profile data in Figure 10a for regularization parameter $\lambda = 5.2983 \times 10^{-4}$. The inverted triangles along the surface $z = 0$ show the locations of SP electrodes in the parallel monitoring array, and the stochastic sources determined by PSO of Equation 5 for the given electrical-potential profile data are shown in the tomograms by the black dots beneath the surface $z = 0$. The north fault is imaged between x-coordinates of about 37–52 m. The location, width,

10.1029/2024WR037549

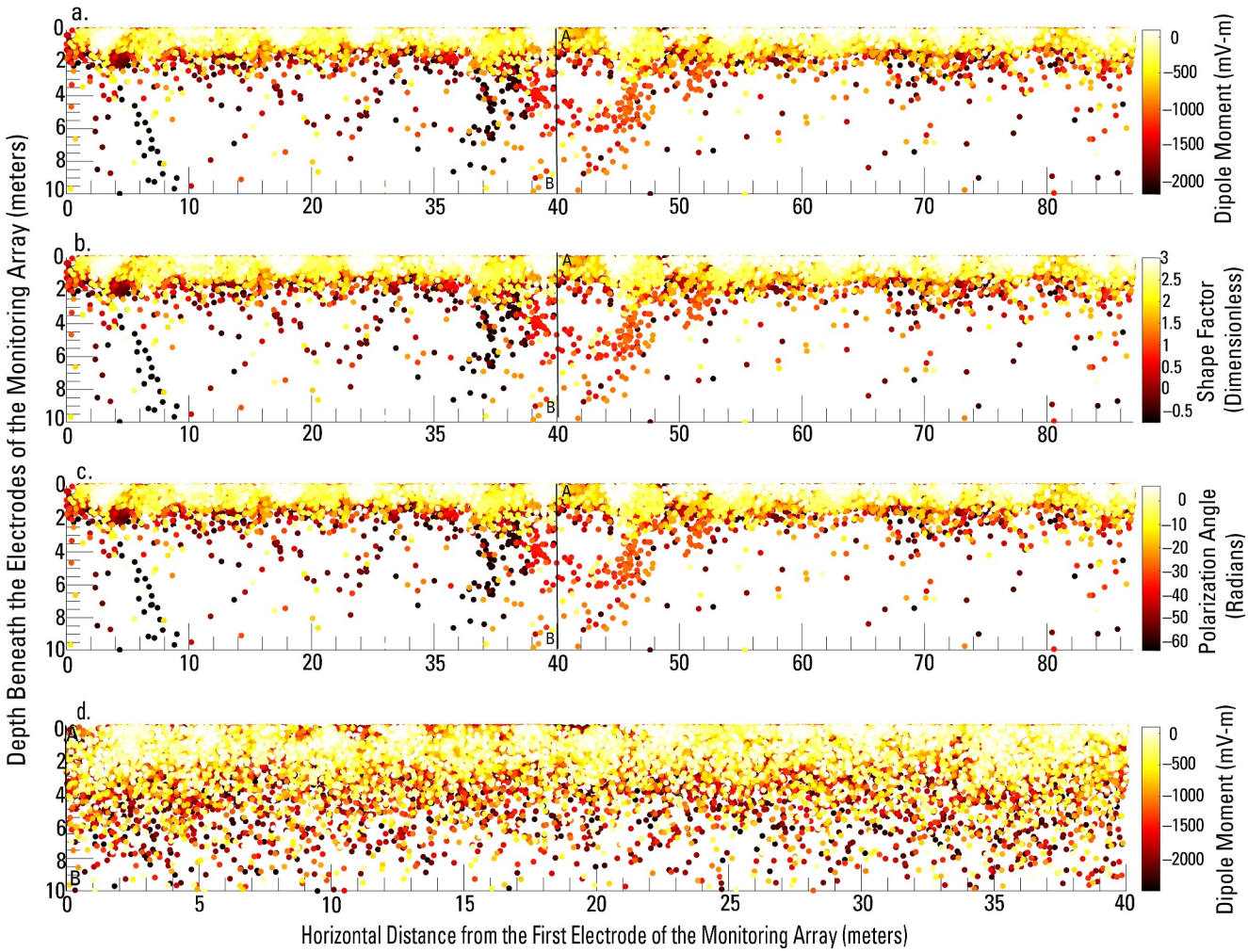

Figure 9. Results of source localization by particle swarm optimization using a maximum of 15 sources for each time-series profile of electrical potential data measured along the monitoring arrays. (a) Inverted values of electric dipole moments beneath the parallel monitoring array. (b) Inverted values of shape factors beneath the parallel monitoring array. (c) Inverted values of polarization angles beneath the parallel monitoring array. (d) Inverted values of electric dipole moments beneath the perpendicular monitoring array. The vertical solid black line A–B indicates the approximate plane of intersection of the parallel and perpendicular arrays.

and geometry of the north fault imaged in Figure 10b is consistent with the location, width, and geometry of the north fault annotated in the resistivity data shown in Figure 7a.

Figure 10c shows an SP tomogram produced by inversion of one profile of electrical-potential data across the perpendicular monitoring array at a single measurement time. The $x = 0$ coordinate of the tomogram corresponds to the intersection of the parallel array at the approximate midpoint of the parallel array. Similar to Figure 10b, the stochastic sources determined by PSO of Equation 5 for the given electrical-potential profile data are shown in the tomograms by the black dots beneath the $z = 0$ surface. The electrical structure and layering in the tomogram in Figure 10c resembles the electrical structure and layering in the accumulated stochastic sources shown in Figure 9d. There is a clear layering between dipole moments of different polarity, which appear to define an ambiguous horizontal boundary between about 4 and 6 m depths beneath the electrodes where the polarity change occurs. It is evident from simultaneous consideration of the tomograms corresponding to the parallel and perpendicular arrays that this layering appears as a preferential flow path between the East Fork stream and the flood plain along the north fault. Note that resistivity heterogeneity can be incorporated into the inversion result by Equation 6 to produce an inverse model of electrical current when collocated resistivity data are available at the model grid nodes. This has been omitted here because there is not an exact alignment between ERT survey lines and either of the SP monitoring arrays, and there is substantial heterogeneity in the flood plain subsurface between the fractured and faulted bedrock, alluvial sediments, and the potential for karst.

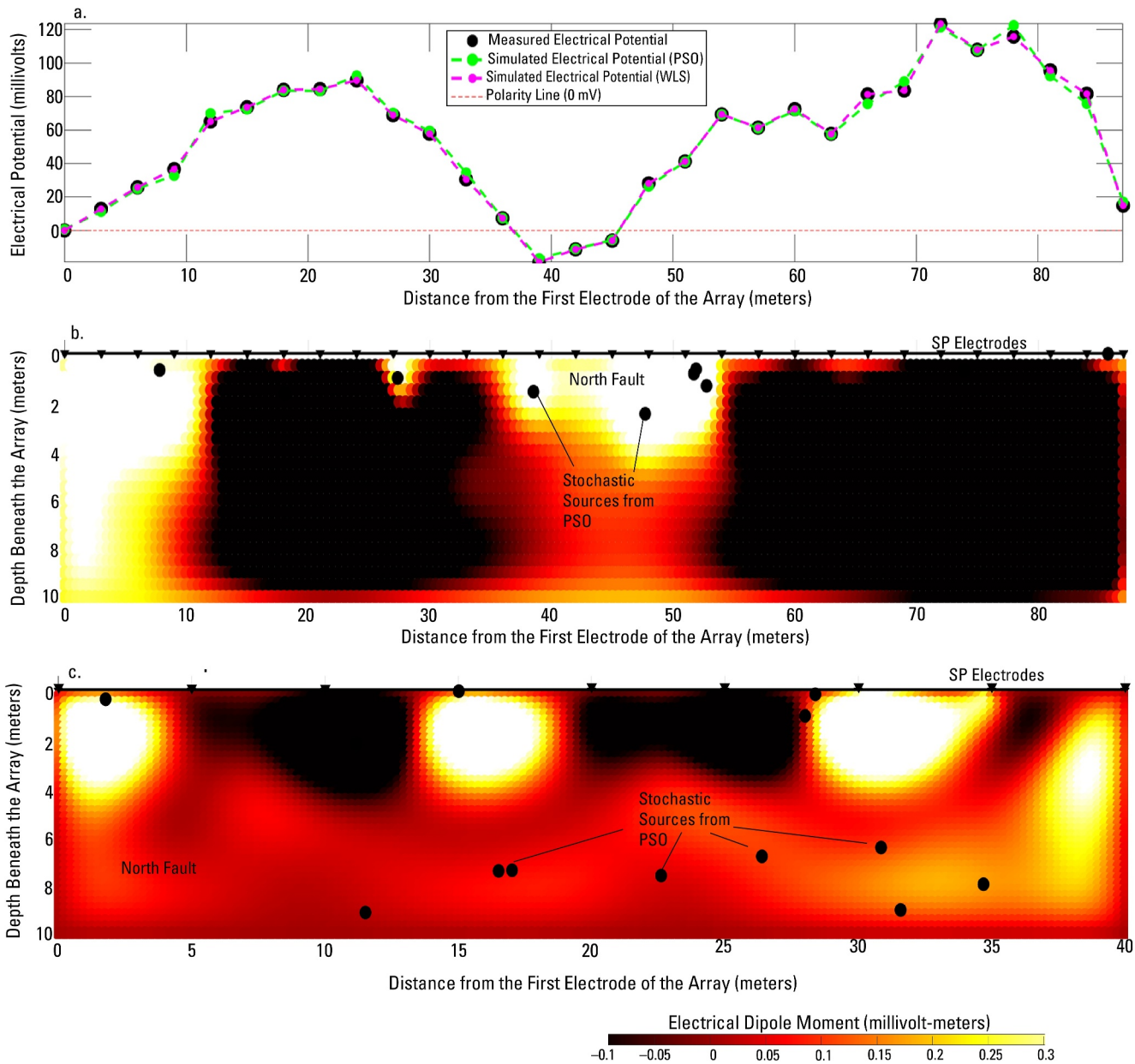

Figure 10. Results of preconditioned source tomography applied to self-potential monitoring data measured at East Fork Poplar creek on the parallel and perpendicular monitoring arrays at a single time. (a) Comparisons of measured electrical-potential data with data simulated by the particle swarm optimization algorithm (green data) and the source tomography algorithm (pink data). (b) Inverted distribution of electric dipole-moments beneath the parallel monitoring array. (c) Inverted distribution of electric dipole-moment beneath the perpendicular monitoring array.

6. Discussion of Results

This section provides a discussion of the results obtained by applying the inversion methodology described in Section 3 to synthetic-model and SP monitoring data. The inverse-modeling algorithm is evaluated for its ability to: (a) locate and image synthetic-model sources and quantify their electrical properties, (b) image the electrical-current sources within the East Fork flood plain from electrical-potential profile data, and (c) capture transient electrical conditions in the East Fork flood plain attributed to hyporheic exchange along the north fault between the stream, flood plain, and the bedrock aquifer.

6.1. Inversion of Synthetic Models

The robust nature of the PSO algorithm used for source localization was demonstrated by inversion of the electrical-source locations from the simulated data derived from the 1-source and 3-source synthetic models contaminated with variable percentages of noise. The PSO algorithm converged on the 1-source synthetic model within 10–35 iterations, accurately located the source, simulated the synthetic-model data with low residual error, and quantified the true electrical properties of the source nearly perfectly for the case with 0% noise (Figure 2). The PSO algorithm also converged and reasonably accurately recovered the location of the source when 5, 10 and 50% noise were added, albeit with reduced accuracy relative to the optimized dipole-moment parameter in the test-case with 50% noise (Figure 2d). Similarly, the PSO algorithm applied to the 3-source synthetic model approximated the locations of the three sources with reasonable accuracy for all levels of noise added to the synthetic-model data (Figure 3). Figure 3 displays minor differences in the optimized locations of the three synthetic sources between the noise-free synthetic data and the synthetic data with 50% noise added. Additionally, Figure 4 indicates that the electrical properties of the three synthetic sources were quantified by PSO with reasonable accuracy because they plotted predominantly around the line $y = x$ in the comparison of inverted and true parameter values for all percentages of noise added to the synthetic-model data. In all test cases for 3-source synthetic models, the relative error (RE) between assigned and simulated Equation 5 parameters reported in Table 1 varied between -135 and $+140$%, with the minimum and maximum values corresponding to the dipole moments of the pink and light-blue synthetic sources, respectively, for the test cases of 50% and 10% added noise, respectively. Excluding these extreme RE values, the mean RE for all other parameters was -7.9% and the median RE value was -2.7%. The RMSE between the simulated model data and the true model data for the optimized parameters varied between 0.0251 and 0.0879 mV for all test cases indicating that the true-model data are reproduced by the simulated data to a microvolt level of residual error for the stochastic-sources that were optimized. In all test cases, the accuracy of simulated parameters could be improved at the expense of computational speed by increasing the number of allotted PSO iterations per stochastic source, reducing the convergence tolerance (which may also inadvertently overfit the data), or increasing the number of particles applied to each particle swarm.

Figure 5 illustrates the improvement imparted into the inverse-model tomograms by the PSO preconditioning step, most prevalently in cases where substantial noise was added to the inverse-modeled data. The tomograms in Figure 5 approximate the locations of the pink and blue synthetic sources in the discretized model space; however, the preconditioned tomography algorithm struggles to image the green source for all percentages of noise, and this may illustrate an inherent limitation in the gradient-based tomography algorithm, as the source location and parameter values are reasonably accurately identified and quantified by the PSO preconditioning step. The reduced performance on 3-source synthetic model in imaging the green synthetic source is primarily attributed the fact that the tomography algorithm produces a spatially continuous parameter field that is attempting to image a single, relatively weak electrical source at a fixed point in the model space, as opposed to a distributed aggregation of sources, which may more realistically represent groundwater flow through a preferential flow path. The green source was assigned the lowest value of dipole-moment intensity of the three synthetic sources, and the dipole-moment provided insufficient signal relative to the assigned dipole-moments of the pink and blue sources and the added noise. Despite the rather poor performance of the tomography algorithm in imaging the green synthetic source, SP source-tomography preconditioned by PSO of Equation 5 appears to be a reasonably valid tool for inverting SP monitoring field data for electrical dipole-moment sources attributed to groundwater flow, which is in many cases one of the strongest primary sources of self-potential in the near subsurface.

6.2. Inversion of the Self-Potential Monitoring Data

Stochastic electrical sources beneath the parallel monitoring array (Figure 9a) plot predominantly between depths of about 0–3 m with source density decreasing at greater depths beneath the array. Sources characterized by positive dipole moment values are primarily constrained to the first 1–2 m beneath the monitoring array. Within this range of depths there is a dense clustering of electrical sources that are characterized by a mix of relatively weak-positive and weak-negative dipole moments between about $+50$ mV · m and -500 mV · m (1–2 orders of magnitude greater than synthetic-model sources). The cluster depicts an electrical layering of sources with consistent dipole-moment intensities that might be a result of water transfer between the stream and the thin veneer of porous alluvial sediments above the bedrock aquifer on the flood plain. Stochastic sources within this region are characterized by shape factors that are predominantly greater than two indicating sources of

predominantly spherical and cylindrical geometry, and polarization angles that are constrained between values of about −5 radians and +5 radians. In contrast, the electrical sources at depths greater than 2 m are characterized by comparatively stronger negative dipole moments between about −500 mV · m and −3,000 mV · m (2–3 orders of magnitude greater than synthetic-model sources), predominantly negative shape factors between about −0.5 and +2.0 indicating a larger proportion of sources with planar sheet-like geometry, and polarization angles between about −10 and −40 radians. Fewer stochastic sources are plotted between depths of 3–10 m compared to between 0 and 2 m, except at x-coordinates between about 35 and 50 m which is the region of the north fault depicted in ERT0 data (Figure 7a) and in the SP tomogram in Figure 10a. The sources within this region, which appear to cluster along one or more inclined vertical planes, likely reflect enhanced hyporheic exchange with the flood plain along the fault through the bedrock streambed, which is visibly fractured in this region (see Figure 1 in Ikard et al. (2023b)). Fewer sources below depths of 2–4 m may result if there is reduced groundwater flow attributed to the closing of fractures and reduced accessibility of karst features at greater depths in the bedrock aquifer. This observation may also reflect the reduced sensitivity of SP data to electrical sources at greater depths. Nevertheless, stochastic sources located between x-coordinates of about 37–52 m on the parallel monitoring array are spatially coincident with the polarity change observed in the WaSP anomaly across the north fault, shown in Figure 7b and show relatively dense clustering at depths greater than 8 m.

Stochastic electrical sources plotted beneath the perpendicular array (Figure 9d) are similar in magnitude to those beneath the parallel array, albeit with some obvious differences in the spatial distribution and electrical layering depicted by the distribution of the sources. In general, electrical sources appear to be deeper beneath the perpendicular array than beneath the parallel array and are more densely clustered between depths of 4–8 m beneath the perpendicular array. Like the stochastic sources depicted in Figure 9a, the stochastic sources in Figure 9d are characterized by predominantly positive dipole moment values between 0 m and about 2 m depth; however, the distribution of stochastic sources characterized by weak-negative dipole moment values between 0 and −500 mV · m appears about 2–3 m thicker beneath the perpendicular array than beneath the parallel array. The comparably denser source clustering at depth beneath the perpendicular array relative to the parallel array may reflect a greater component of preferential groundwater flow into the flood plain at greater depths, which may occur as a result of lateral and vertical flow along a fracture or fault plane.

The electric dipole moment is a vector quantity with direction that points from the negative charge toward the positive charge. A change in direction of the dipole-moment vector therefore results in a change in polarity attributed to the change in direction of charge separation, which can occur in response to a change in groundwater-flow direction. Figure 11 aligns the tomograms in Figure 10 and rotates the view to depict the differences in electrical polarity in the subsurface at the intersection of the north fault and the East Fork streambed. Figure 11a shows an electrical condition where the inverted electrical dipole moments near the intersection of the north fault and the stream are predominantly negative polarity. Figure 11b shows the opposite electrical condition where inverted electrical dipole moments in the subsurface near the north fault are predominantly positive polarity. These transient electrical dynamics are at times attributed to water transfers between the stream and the fault, as can be inferred by the comparison of streamflow from gage EF5.4K (310 m upstream from the SP monitoring arrays) to measured voltages and calculated electrical potentials on the flood plain and inverted electrical sources at selected locations beneath the monitoring arrays, shown in Figure 12.

The graphs in Figure 12 demonstrate that a relation exists between streamflow in East Fork and the measured and inverted SP monitoring data. In Figure 12a, streamflow data (blue) measured during a period of elapsed time of 60–110 days are compared to voltages at selected electrodes on the parallel array upstream from the north fault (electrode 3, green), on top of the fault (electrode 15, black), and downstream from the fault (electrode 25, pink). In Figure 12b, the relation between streamflow data and electrical-potential time-series on each of the selected electrodes in Figure 12a is depicted. Figure 12c depicts the relation between streamflow and time-series of inverted dipole moment sources at different depths beneath the selected electrodes. Clear dependencies of the measured voltages, electrical-potential, and inverted dipole moments on discrete stormflow discharge events in East Fork are evident between about 77 and 100 days. Following a period of relatively low and consistent streamflow between 60 and 77 days that is characterized by linearly drifting voltages, electrical-potential, and dipole-moment sources, a discrete increase in streamflow at 77 days is synced in time to notable changes in the monitored and inverted self-potential data. The electrical conditions at and beneath the corresponding electrodes change noticeably in response to successive streamflow events within the displayed time period. In contrast, the

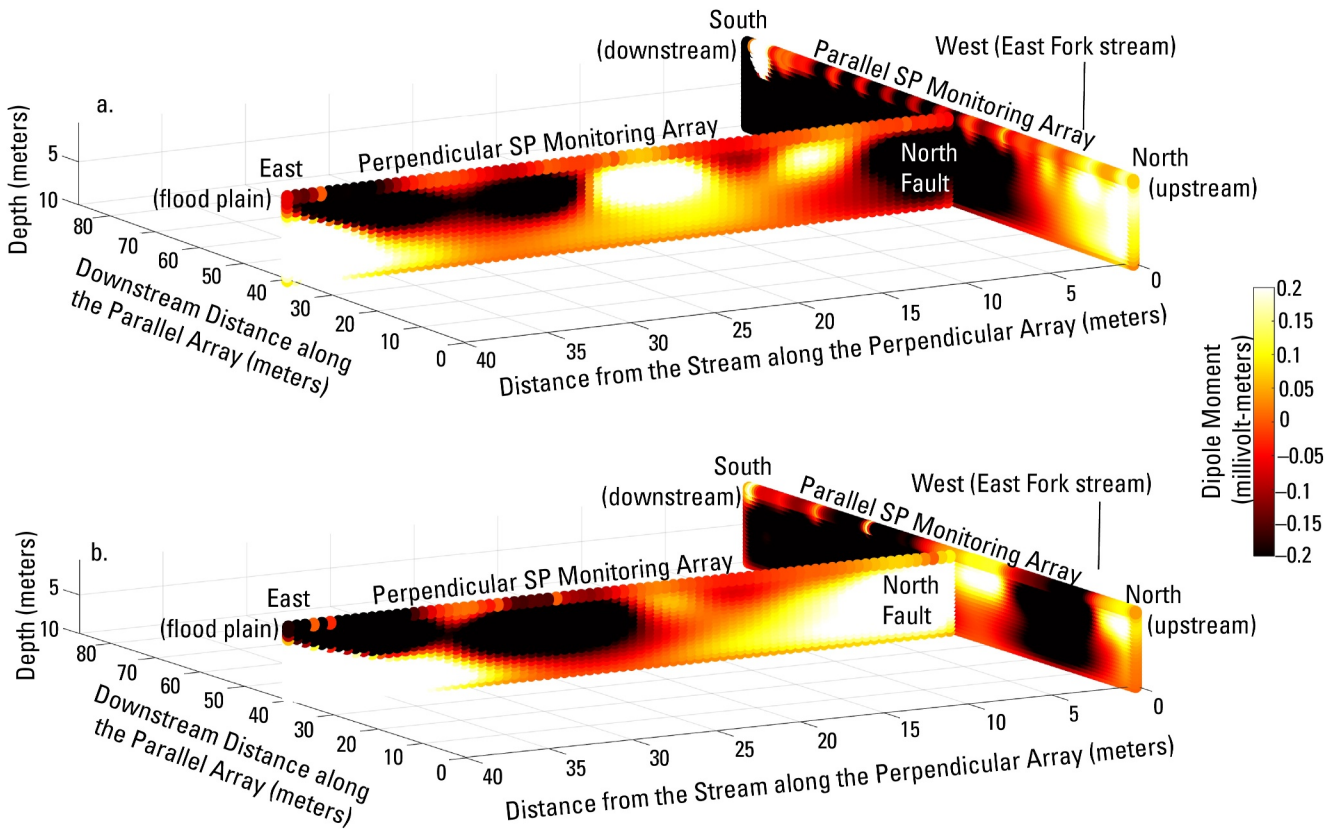

Figure 11. Results of source tomography from self-potential monitoring data measured at East Fork Poplar creek on the parallel and perpendicular monitoring arrays at two different times representing gaining and losing conditions as indicated by the polarity of the inverted dipole moments in the subsurface near the north fault. (a) Inverted distribution of electric dipole moments showing negative dipole moments in the subsurface near the north fault. (b) Inverted distribution of electric dipole moments showing positive dipole moments in the subsurface near the north fault.

dependency between streamflow and inverted dipole-moment sources beneath electrode 3 (green, upstream from the north fault) is less apparent.

Figure 13 depicts transient changes of the inverted dipole-moment sources in the East Fork flood plain that are attributed to streamflow losing conditions along the north fault at five successive times. Inverted dipole-moment sources beneath the perpendicular monitoring array increase through time progressively further outward from the stream onto the flood plain in Figures 13a–13c. Figures 13d and 13e depict a contraction and attenuation of the dipole-moment sources around the intersection of the monitoring arrays. The dipole moments observed at 20–25 m along the perpendicular array in Figure 13c appear to progressively diminish and spread further laterally and vertically deeper into the flood plain, extending 30–35 m into the flood plain and reaching depths of 8–10 m beneath the surface. These results demonstrate that spatiotemporal SP monitoring and inversion elucidates changes in the size, location, and configuration of the active-flow region of the hyporheic zone along the north fault through time. This represents a valuable methodological development and addition to established methods for investigating groundwater and surface-water exchange (temperature sensing, WaSP surveying, tracer methods, wells), which provide data that is fairly continuous spatially and over time but do not directly examine the subsurface in this manner. SP monitoring and inversion by the methodologies described herein therefore present a new method for monitoring groundwater and surface-water exchange and characterizing hyporheic zones in bedrock rivers, both spatially and temporally.

7. Conclusions

Self-potential source-localization and source-tomography were combined into an algorithm to inverse model spatially distributed SP monitoring data measured on the flood plain of a bedrock river. Source localization was performed by PSO of an analytical forward model of horizontal electrical-potential profile data attributed to

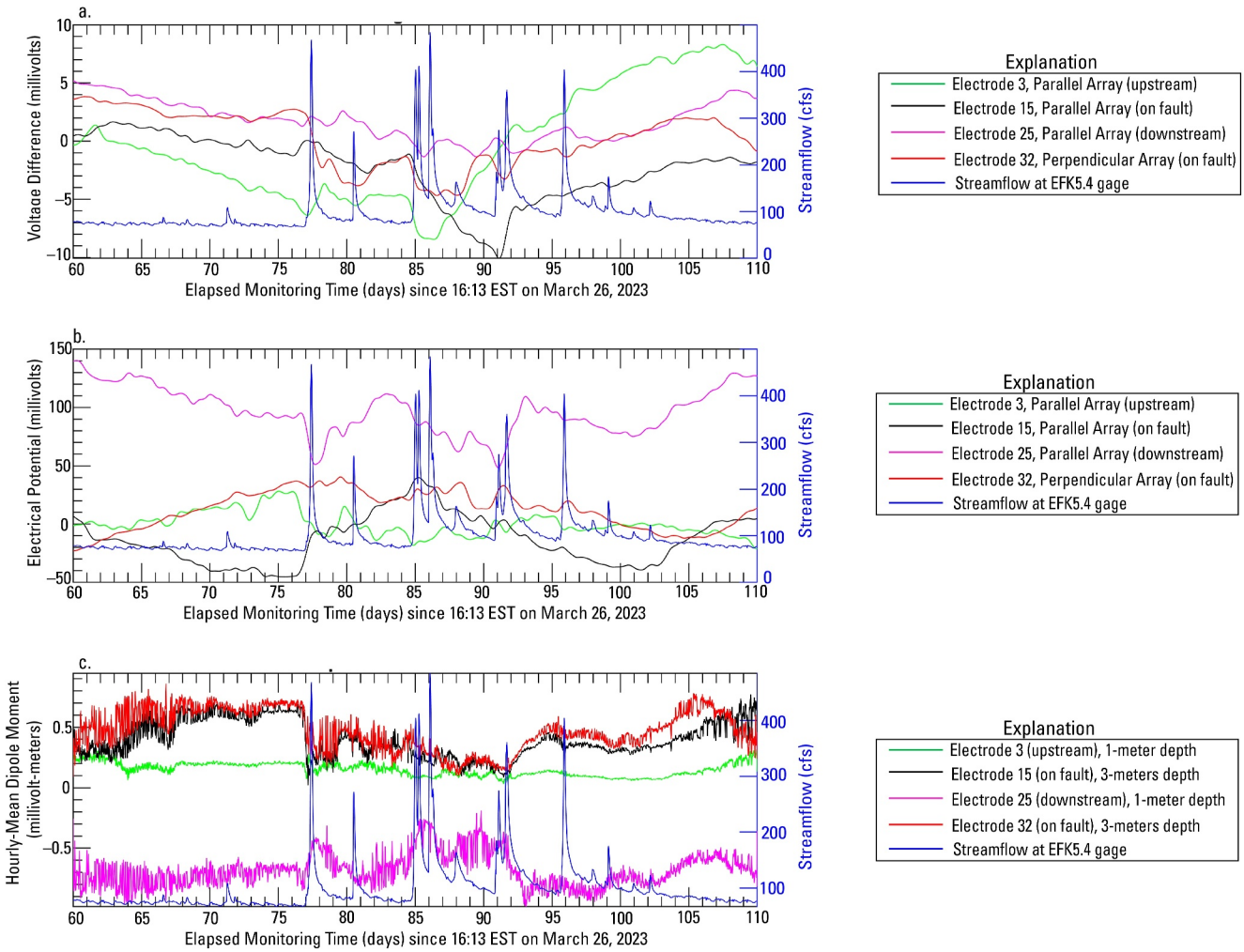

Figure 12. Comparison of streamflow at gage EF5.4K to (a) measured voltages at selected electrodes on the self-potential monitoring arrays, (b) electrical potential times-series calculated from measured voltages, and (c) inverted electrical dipole-moment sources at different depths within the East Fork flood plain inverted from spatial profiles of electrical potential. The comparisons illustrate a dependency between streamflow, measured voltages, calculated electrical-potential, and inverted dipole-moment sources.

buried electrical sources with simple geometries. Source tomography was performed by regularized WLS regression. The two algorithms were combined by preconditioning the WLS objective function with prior information on positions and dipole-moment intensities of stochastic electrical sources optimized by PSO. The inversion algorithm was tested on 1-source and 3-source synthetic models with 0%, 5%, 10%, and 50% added noise, and then applied to SP monitoring data measured along two intersecting electrode arrays oriented parallel and perpendicular to a previously identified fault through the bedrock riverbed and flood plain of East Fork Poplar Creek. Such a tool contributes to several pressing needs in the hydrogeophysical sciences: (1) the need for data-processing tools to expand upon methodologies available for characterization of bedrock rivers, (2) the need to be able to monitor and quantify the relative changes in hyporheic exchange in bedrock and alluvial rivers through time to gain better understanding of hyporheic zone processes in both bedrock and alluvial rivers, and (3) the need for accessible and computationally efficient and robust SP-data inversion algorithms for general practice in hydrogeophysical sciences. Several novel advances are offered by this work through addressing these needs, including: (1) a practical and efficient inversion algorithm for two-dimensional inversion of waterborne and land-based self-potential data, (2) a modification to the PSO algorithm to sequentially localize and optimize the electrical properties of any specified number of stochastic sources, (3) a modification of the gradient-based SP tomography algorithm to (a) incorporate the PSO algorithm as a preconditioning step and (b) incorporate an analytical model that relinquishes the need to solve the coupled groundwater-flow and electrostatic partial

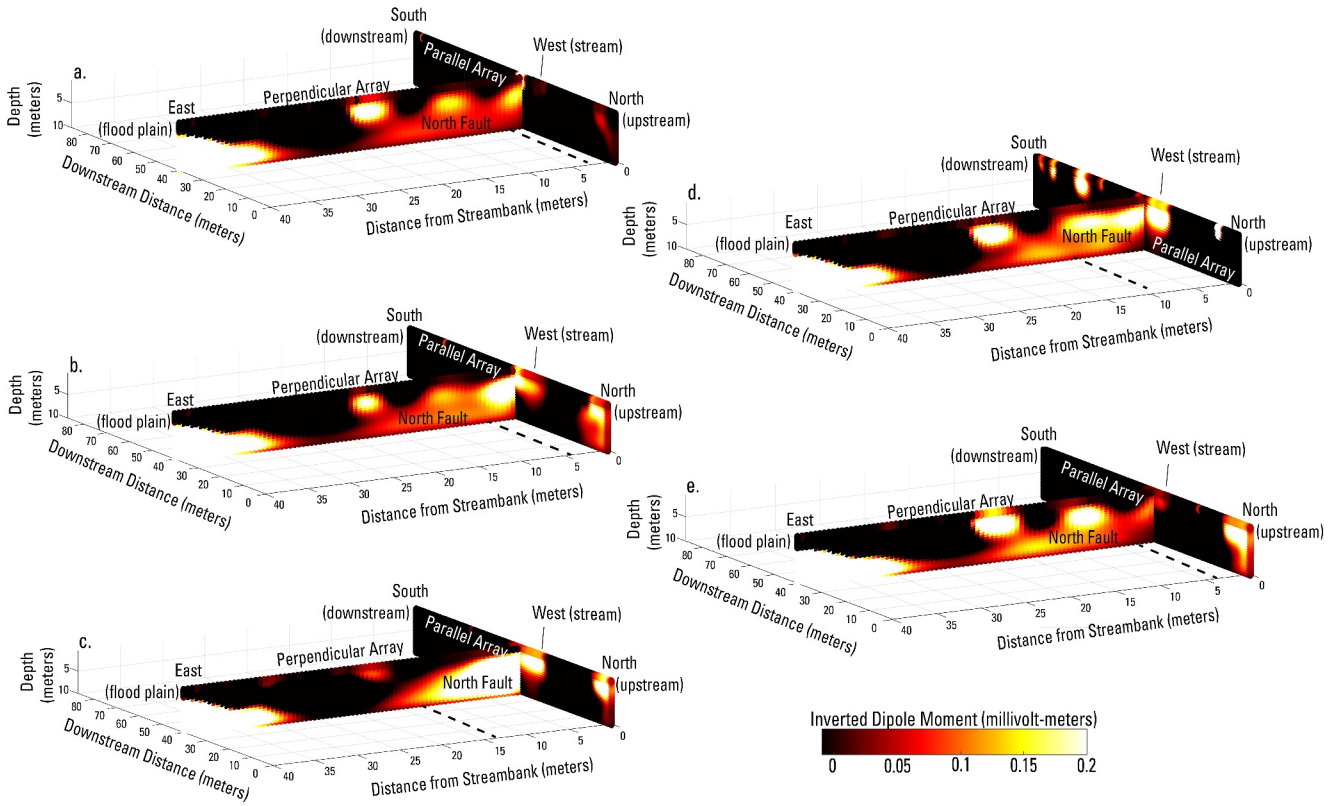

Figure 13. Transient electrical changes of inverted dipole-moment sources in the East Fork flood plain along the north fault attributed to streamflow losing conditions at five successive times. Dipole-moments were calculated by inversion of spatial profiles of electrical-potential along the monitoring arrays that were calculated through time from the voltage time-series measured on each SP electrode.

differential equations. These advances eliminate inherent assumptions as to the nature of the inverted electrical sources (streaming-current vs. diffusion etc.), and demonstrate an application of time-lapse SP monitoring to image hyporheic exchange in a bedrock river through time, which has not been previously investigated through SP monitoring.

Data Availability Statement

The SP monitoring data, water-quality monitoring data, streamflow data, data-processing and SP inversion software, and the output SP inversion-model data pertaining to the analysis described herein, are available online as a U.S. Geological Survey data release by Ikard et al. (2024). Additional supporting waterborne self-potential and electrical resistivity tomography data sets are available as a U.S. Geological Survey data release by Ikard et al. (2022) and Ikard et al. (2023b).

Acknowledgments

This work was supported by Department of Energy Minority Serving Institution Partnership Program (MSIPP) managed by the Savannah River National Laboratory under BSRA contract TOA 0000525176. Additional support was provided by the U. S. Department of Energy, Office of Science, Biological and Environmental Research - Research and Development Partnership Pilots (DE-SC0023132) and is a product of the Watershed Dynamics and Evolution Science Focus Area at Oak Ridge National Laboratory. Oak Ridge National Laboratory is managed by UT-Battelle, LLC, for the U.S. Department of Energy under contract DE-AC05-00OR22725. The authors wish to thank the peer-reviewers for assistance in improving this research. Any use of trade, firm, or product names is for descriptive purposes only and does not imply endorsement by the U.S. Government.

References

Anderson, M. P., Woessner, W. W., & Hunt, R. J. (2015). *Applied groundwater modeling—simulation of flow and advective transport* (2nd ed.). Elsevier. (p. 564). https://doi.org/10.1016/C2009-0-21563-7

Aster, R. C., Borchers, B., & Thurber, C. H. (2005). *Parameter estimation and inverse problems*. Elsevier. (p. 301). https://doi.org/10.1016/C2009-0-61134-X

Babu, H. V. R., & Rao, D. A. (1988). A rapid graphical method for the interpretation of the self-potential anomaly over a two-dimensional inclined sheet of finite depth extent. *Geophysics*, *53*(8), 1126–1128. https://doi.org/10.1190/1.1442551

Banerjee, B. (1971). Quantitative interpretation of self-potential anomalies of some specific geometric bodies. *Pure and Applied Geophysics*, *90*(1), 138–152. https://doi.org/10.1007/BF00875518

Barde-Cabusson, S., Finizola, A., & Grobbe, N. (2021). A practical approach for self-potential data acquisition, processing, and visualization. *Interpretation*, *9*(1), 123–143. https://doi.org/10.1190/INT-2020-0012.1

Bencala, K. E. (2005). Hyporheic exchange flows. In M. G. Anderson & J. J. McDonnell (Eds.), *Encyclopedia of hydrological sciences*. John Wiley and Sons, Ltd. https://doi.org/10.1002/0470848944.hsa126

Bhattacharya, B. B., & Roy, N. A. (1981). A note on the use of a nomogram for self-potential anomalies. *Geophysical Prospecting*, *29*(1), 102–107. https://doi.org/10.1111/j.1365-2478.1981.tb01013.x

Biswas, A. (2016). A comparative performance of least-square method and very fast simulated annealing global optimization method for interpretation of self-potential anomaly over 2-D inclined sheet type structure. *Journal of the Geological Society of India*, *88*(4), 493–502. https://doi.org/10.1007/s12594-016-0512-8

Biswas, A., & Sharma, S. P. (2014a). Optimization of self-potential interpretation of 2-D inclined sheet-type structures based on very fast simulated annealing and analysis of ambiguity. *Journal of Applied Geophysics*, *105*, 235–247. https://doi.org/10.1016/j.jappgeo.2014.03.023

Biswas, A., & Sharma, S. P. (2014b). Resolution of multiple sheet-type structures in self-potential measurement. *Journal of Earth Systems Sciences*, *123*(4), 809–825. https://doi.org/10.1007/s12040-014-0432-1

Biswas, A., & Sharma, S. P. (2015). Interpretation of self-potential anomaly over idealized bodies and analysis of ambiguity using very fast simulated annealing global optimization technique. *Near Surface Geophysics*, *13*(2), 179–195. https://doi.org/10.3997/1873-0604.2015005

Blakely, R. J. (1995). *Potential theory in gravity and magnetic applications* (1st ed.). Cambridge University Press. (p. 441). https://doi.org/10.1017/CBO9780511549816

Bolève, A., Revil, A., Janod, F., Mattiuzzo, J. L., & Jardani, A. (2007). Forward Modeling and validation of a new formulation to compute self-potential signals associated with groundwater flow. *Hydrology and Earth System Sciences*, *11*(5), 1661–1671. https://doi.org/10.5194/hess-11-1661-2007

Cardenas, M. B., & Gooseff, M. N. (2008). Comparison of hyporheic exchange under covered and uncovered channels based on linked surface and groundwater flow simulations. *Water Resources Research*, *44*(3), 1–11. https://doi.org/10.1029/2007WR006506

Chow, R., Parker, B. L., Steelman, C. M., Thoms, A., & Nowak, W. (2021). How do fractures influence hyporheic exchange in sedimentary rock riverbeds? *Water Resources Research*, *57*(7), 1–15. https://doi.org/10.1029/2020WR028476

Crespy, A., Revil, A., Linde, N., Byrdina, S., Jardani, A., Bolève, A., & Henry, P. (2008). Detection and localization of hydromechanical disturbances in a sandbox using the self-potential method. *Journal of Geophysical Research*, *113*(B1), 1–23. https://doi.org/10.1029/2007JB005042

Di Maio, R., Piegari, E., Payal, R., Carbonari, R., Vitagliano, E., & Milano, L. (2019). Quantitative interpretation of multiple self-potential anomaly sources by a global optimization approach. *Journal of Applied Geophysics*, *162*, 152–163. https://doi.org/10.1016/j.jappgeo.2019.02.004

Eberhart, R., & Kennedy, J. (1995). A new optimizer using particle swarm theory. In *MHS'95—proceedings of the sixth international symposium on micro machine and human science* (pp. 39–43). https://doi.org/10.1109/MHS.1995.494215

Elhussein, M. (2021). A novel approach to self-potential data interpretation in support of mineral resource development. *Natural Resources Research*, *30*(1), 97–127. https://doi.org/10.1007/s11053-020-09708-1

El-Kaliouby, H. M., & Al-Garni, M. A. (2009). Inversion of self-potential anomalies caused by 2D inclined sheets using neural networks. *Journal of Geophysics and Engineering*, *6*(1), 29–34. https://doi.org/10.1088/1742-2132/6/1/003

Essa, K., Mehanee, S., & Smith, P. D. (2008). A new inversion algorithm for estimating the best fitting parameters of some geometrically simple body to measured self-potential anomalies. *Exploration Geophysics*, *39*(3), 155–163. https://doi.org/10.1071/EG08017

Essa, K. S. (2019). A particle swarm optimization method for interpreting self-potential anomalies. *Journal of Geophysics and Engineering*, *16*(2), 463–477. https://doi.org/10.1093/jge/gxz024

Essa, K. S. (2020). Self-potential data interpretation utilizing the particle swarm method for the finite 2D inclined dike—Mineralized zones delineation. *Acta Geodaetica et Geophysica*, *55*(2), 203–221. https://doi.org/10.1007/s40328-020-00289-2

Essa, K. S., & Elhussein, M. (2017). A new approach for the interpretation of self-potential data by 2-D inclined plate. *Journal of Applied Geophysics*, *136*, 455–461. https://doi.org/10.1016/j.jappgeo.2016.11.019

Essa, K. S., & Elhussein, M. (2018). PSO (particle swarm optimization) for interpretation of magnetic anomalies caused by simple geometrical structures. *Pure and Applied Geophysics*, *175*(10), 3539–3553. https://doi.org/10.1007/s00024-018-1867-0

Essa, K. S., & Elhussein, M. (2020). Interpretation of magnetic data through particle swarm optimization—Mineral exploration case studies. *Natural Resources Research*, *29*(1), 521–537. https://doi.org/10.1007/s11053-020-09617-3

Fernández-Martínez, J. L., García-Gonzalo, E., & Naudet, V. (2010). Particle swarm optimization applied to solving and appraising the streaming-potential inverse problem. *Geophysics*, *75*(4), 3–15. https://doi.org/10.1190/1.3460842

Findlay, S. (1995). Importance of surface-subsurface exchange in stream ecosystems—The hyporheic zone. *Limnology & Oceanography*, *40*(1), 159–164. https://doi.org/10.4319/lo.1995.40.1.0159

Gobashy, M., Abdelazeem, M., Abdrabou, M., & Khalil, M. H. (2020). Estimating model parameters from self-potential anomaly of 2D inclined sheet using the whale optimization algorithm—Applications to mineral exploration and tracing shear zones. *Natural Resources Research*, *29*(1), 499–519. https://doi.org/10.1007/s11053-019-09526-0

Göktürkler, G., & Balkaya, Ç. (2012). Inversion of self-potential anomalies caused by simple-geometry bodies using global optimization algorithms. *Journal of Geophysics and Engineering*, *9*(5), 498–507. https://doi.org/10.1088/1742-2132/9/5/498

Griffiths, D. J. (1999). *Introduction to electrodynamics* (3rd ed., p. 576p). Prentice Hall.

Haas, A. K., Revil, A., Karaoulis, M., Frash, L., Hampton, J., Gutierrez, M., & Mooney, M. (2013). Electric potential source localization reveals a borehole leak during hydraulic fracturing. *Geophysics*, *78*(2), 93–113. https://doi.org/10.1190/geo2012-0388.1

Hansen, P. C., & O'Leary, D. P. (1993). The use of the L-curve in the regularization of discrete Ill-posed problems. *SIAM Journal on Scientific Computing*, *14*(6), 1487–1503. https://doi.org/10.1137/0914086

Harvey, J., & Gooseff, M. (2015). River corridor science—Hydrologic exchange and ecological consequences from bedforms to basins. *Water Resources Research*, *51*(9), 6893–6922. https://doi.org/10.1002/2015WR017617

Ikard, S. J., Briggs, M. A., & Lane, J. W. (2021). Investigation of scale-dependent groundwater/surface-water exchange in rivers by gradient self-potential logging—Numerical modeling and field experiments. *Journal of Environmental & Engineering Geophysics*, *26*(2), 83–98. https://doi.org/10.32389/JEEG20-066

Ikard, S. J., Carroll, K. C., Books, S. C., Smith-Vega, G., Elwes, A., & Rucker, D. F. (2024). Self-potential tomography preconditioned by particle swarm optimization—Self-potential monitoring and streamflow data acquired March 26–September 14, 2023 at East Fork Poplar Creek near Oak Ridge Tennessee, with forward and inverse modeling computer scripts [Dataset]. *U.S. Geological Survey data release*. https://doi.org/10.5066/P9ASZNJR

Ikard, S. J., Carroll, K. C., Rucker, D. F., Adams, R. F., & Brooks, S. C. (2023b). Geoelectric characterization of hyporheic exchange flow in the bedrock-lined streambed of East Fork Poplar Creek, Oak Ridge, Tennessee. *Geophysical Research Letters*, *50*(8), 1–11. https://doi.org/10.1029/2022GL102616

Ikard, S. J., Carroll, K. C., Rucker, D. F., Teeple, A. P., Tsai, C. H., Payne, J. D., et al. (2023a). Geoelectric monitoring of the electric potential field of the lower Rio Grande before during and after intermittent streamflow, May–October, 2022. *Water*, *15*(9), 1–47. https://doi.org/10.3390/w15091652

Ikard, S. J., Minsley, B. J., Rigby, J. R., & Kress, W. K. (2023c). A model of transmissivity and hydraulic conductivity from electrical resistivity distribution derived from airborne electromagnetic surveys of the Mississippi River Valley alluvial aquifer, Midwest USA. *Hydrogeology Journal*, *31*(2), 313–334. https://doi.org/10.1007/s10040-022-02590-6

Ikard, S. J., & Revil, A. (2014). Self-potential monitoring of a thermal pulse advecting through a preferential flow path. *Journal of Hydrology*, *519*(A), 34–49. https://doi.org/10.1016/j.jhydrol.2014.07.001

Ikard, S. J., Revil, A., Jardani, A., Woodruff, W. W., Parekh, M., & Mooney, M. (2012). A saline pulse test monitored by the self-potential method to non-intrusively determine the velocity of the pore water in leaking areas of earth dams and embankments. *Water Resources Research*, *48*(4), 1–17. https://doi.org/10.1029/2010WR010247

Ikard, S. J., Rucker, D. F., Carroll, K. C., Adams, R. F., & Perez, G. M. (2022). Waterborne self-potential data, surface-water temperature and conductivity logging data, and electric resistivity tomography data measured at East Fork Poplar Creek, Oak Ridge, Tennessee, January-March 2022 [Dataset]. *U.S. Geological Survey data release*. https://doi.org/10.5066/P9BAW75G

Ikard, S. J., Teeple, A. P., & Humberson, D. H. (2021). Gradient self-potential logging in the Rio Grande to identify gaining and losing reaches across the Mesilla Valley. *Water*, *13*(10), 1–23. https://doi.org/10.3390/w13101331

Ikard, S. J., Teeple, A. P., Payne, J. D., Stanton, G. P., & Banta, J. R. (2018). New insights on scale-dependent surface-groundwater exchange from a floating self-potential dipole. *Journal of Environmental & Engineering Geophysics*, *23*(2), 261–287. https://doi.org/10.2113/JEEG23.2.261

Jardani, A., & Revil, A. (2009). Stochastic joint inversion of temperature and self-potential data. *Geophysical Journal International*, *179*(1), 640–654. https://doi.org/10.1111/j.1365-246X.2009.04295.x

Jardani, A., Revil, A., Barrash, W., Crespy, A., Rizzo, E., Straface, S., et al. (2009). Reconstruction of the water table from self-potential data: A Bayesian approach. *Ground Water*, *47*(2), 213–227. https://doi.org/10.1111/j.1745-6584.2008.00513.x

Jardani, A., Revil, A., Bolève, A., Crespy, A., Dupont, J.-P., Barrash, W., & Malama, B. (2007a). Tomography of the Darcy velocity from self-potential measurements. *Geophysical Research Letters*, *34*(24), 1–6. https://doi.org/10.1029/2007GL031907

Jardani, A., Revil, A., Bolève, A., & Dupont, J. P. (2008). Three-dimensional inversion of self-potential data used to constrain the pattern of groundwater flow in geothermal fields. *Journal of Geophysical Research*, *113*(B9), 1–22. https://doi.org/10.1029/2007JB005302

Jardani, A., Revil, A., Santos, F., Fauchard, C., & Dupont, J. P. (2007b). Detection of preferential infiltration pathways in sinkholes using joint inversion of self-potential and EM-34 conductivity data. *Geophysical Prospecting*, *55*(5), 749–760. https://doi.org/10.1111/j.1365-2478.2007.00638.x

Jouniaux, L., Maineult, A., Naudet, V., Pessel, M., & Sailhac, P. (2009). Review of self-potential methods in hydrogeophysics. *Comptes Rendus Geoscience*, *341*(10–11), 928–936. https://doi.org/10.1016/j.crte.2009.08.008

Kalbus, E., Reinstorf, F., & Schirmer, M. (2006). Measuring methods for groundwater – Surface water interactions—A review. *Hydrology and Earth System Sciences*, *10*(6), 873–887. https://doi.org/10.5194/hess-10-873-2006

Kennedy, C. S. C. (2017). *Groundwater-surface water interactions in the discrete fracture networks of bedrock rivers (Doctoral dissertation)*. University of Guelph. Retrieved from https://atrium.lib.uoguelph.ca/items/de60428d-eb26-4593-bf6b-2feff765e537

Krause, S., Hannah, D. M., Fleckenstein, J. H., Heppell, C. M., Kaeser, D., Pickup, R., et al. (2011). Inter-disciplinary perspectives on processes in the hyporheic zone. *Ecohydrology*, *4*(4), 481–499. https://doi.org/10.1002/eco.176

LeVeque, R. J. (2007). *Finite difference methods for ordinary and partial differential equations—steady-state and time-dependent problems* (p. 341). Society for Industrial and Applied Mathematics.

Li, Y., & Oldenburg, D. W. (1996). 3-D inversion of magnetic data. *Geophysics*, *61*(2), 394–408. https://doi.org/10.1190/1.1443968

Li, Y., & Oldenburg, D. W. (1998). 3-D inversion of gravity data. *Geophysics*, *63*(1), 109–119. https://doi.org/10.1190/1.1444302

Li, Y., & Oldenburg, D. W. (2000). 3-D inversion of induced polarization data. *Geophysics*, *65*(6), 1931–1945. https://doi.org/10.1190/1.1444877

Linde, N., Doetsch, J., Jougnot, D., Genoni, O., Dürst, Y., Minsley, B. J., et al. (2011). Self-potential investigations of a gravel bar in a restored river corridor. *Hydrology and Earth System Sciences*, *15*(3), 729–742. https://doi.org/10.5194/hess-15-729-2011

Luo, Y., Du, X., Cui, Y., Guo, Y., Xie, J., & Liu, J. (2023). Inversion of self-potential source based on particle swarm optimization. *Geophysical Prospecting*, *71*(2), 322–335. https://doi.org/10.1111/1365-2478.13299

Martínez-Pagán, P., Jardani, A., Revil, A., & Haas, A. K. (2010). Self-potential monitoring of a salt plume. *Geophysics*, *75*(4), 17–25. https://doi.org/10.1190/1.3475533

Mehanee, S. A. (2022). Simultaneous joint inversion of gravity and self-potential data measured along a profile— Theory, numerical examples, and a case study from mineral exploration with cross validation from electromagnetic data. *IEEE Transactions on Geoscience and Remote Sensing*, *60*, 1–20. https://doi.org/10.1109/TGRS.2021.3071973

Mendonça, C. A. (2008). Forward and inverse self-potential modeling in mineral exploration. *Geophysics*, *73*(1), 33–43. https://doi.org/10.1190/1.2821191

Menke, W. (1989). Geophysical data analysis—Discrete inverse theory (revised edition). In *International geophysics series 45*. Academic Press. (p. 289). https://doi.org/10.1016/B978-0-12-490920-5.X5001-7

Minsley, B. J., Sogade, J., & Morgan, F. D. (2007a). Three-dimensional self-potential inversion for subsurface DNAPL contaminant detection at the Savannah River Site, South Carolina. *Water Resources Research*, *43*(4), 1–13. https://doi.org/10.1029/2005WR003996

Minsley, B. J., Sogade, J., & Morgan, F. D. (2007b). Three-dimensional source inversion of self-potential data. *Journal of Geophysical Research*, *112*(B2), 1–13. https://doi.org/10.1029/2006JB004262

Mitchell, J. K. (1991). Conduction phenomena—From theory to geotechnical practice. *Géotechnique*, *43*(3), 299–340. https://doi.org/10.1680/geot.1991.41.3.299

Mohamed, R. A. M., Brooks, S. C., Tsai, C.-H., Ahmed, T., Rucker, D. F., Ulery, A. L., et al. (2021a). Geostatistical interpolation of streambed hydrologic attributes with addition of left censored data and anisotropy. *Journal of Hydrology*, *599*, 1–16. https://doi.org/10.1016/j.jhydrol.2021.126474

Mohamed, R. A. M., Gabrielli, C., Selker, J. S., Selker, F., Brooks, S. C., Ahmed, T., & Carroll, K. C. (2021b). Comparison of fiber-optic distributed temperature sensing and high-sensitivity sensor spatial surveying of stream temperature. *Journal of Hydrology*, *603*, 1–13. https://doi.org/10.1016/j.jhydrol.2021.127015

Monteiro Santos, F. A. (2010). Inversion of self-potential of idealized bodies' anomalies using particle swarm optimization. *Computers & Geosciences*, *36*(9), 1185–1190. https://doi.org/10.1016/j.cageo.2010.01.011

Nyquist, J. E., & Corry, C. E. (2002). Self-potential–The ugly duckling of environmental geophysics. *The Leading Edge*, *21*(5), 446–451. https://doi.org/10.1190/1.1481251

Oldenburg, D. W., & Li, Y. (1994). Subspace linear inverse method. *Inverse Problems*, *10*(4), 915–935. https://doi.org/10.1088/0266-5611/10/4/011

Oliveti, I., & Cardarelli, E. (2019). Self-potential data inversion for environmental and hydrogeological investigations. *Pure and Applied Geophysics*, *176*(8), 3607–3628. https://doi.org/10.1007/s00024-019-02155-x

Oxtobee, J. P. A., & Novakowski, K. S. (2002). A field investigation of groundwater/surface water interaction in a fractured bedrock environment. *Journal of Hydrology*, *269*(3–4), 169–193. https://doi.org/10.1016/S0022-1694(02)00213-5

Oxtobee, J. P. A., & Novakowski, K. S. (2003). Groundwater/surface water interaction in a fractured rock aquifer. *Ground Water*, *41*(5), 667–681. https://doi.org/10.1111/j.1745-6584.2003.tb02405.x

Pekşen, E., Yas, T., Kayman, A. Y., & Özkan, C. (2011). Application of particle swarm optimization on self-potential data. *Journal of Applied Geophysics*, *75*(2), 305–318. https://doi.org/10.1016/j.jappgeo.2011.07.013

Rao, D. A., & Babu, H. V. R. (1983). Quantitative interpretation of self-potential anomalies due to two-dimensional sheet-like bodies. *Geophysics*, *48*(12), 1659–1664. https://doi.org/10.1190/1.1441446

Revil, A., Ahmed, A. S., & Jardani, A. (2017). Self-potential: A non-intrusive ground water flow sensor. *Journal of Environmental & Engineering Geophysics*, *22*(3), 235–247. https://doi.org/10.2113/JEEG22.3.235

Revil, A., & Jardani, A. (2013). *The self-potential method: Theory and applications in environmental geosciences*. Cambridge University Press.

Revil, A., Karaoulis, M., Johnson, T., & Kemna, A. (2012). Review—Some low-frequency electrical methods for subsurface characterization and monitoring in hydrogeology. *Hydrogeology Journal*, *20*(4), 617–658. https://doi.org/10.1007/s10040-011-0819-x

Revil, A., & Leroy, P. (2001). Hydroelectric coupling in a clayey material. *Geophysical Research Letters*, *28*(8), 1643–1646. https://doi.org/10.1029/2000GL012268

Revil, A., & Leroy, P. (2004). Constitutive equations for ionic transport in porous shales. *Journal of Geophysical Research*, *109*(B3), 1–19. https://doi.org/10.1029/2003JB002755

Revil, A., Leroy, P., & Titov, K. (2005). Characterization of transport properties of argillaceous sediments. Application to the Callovo-Oxfordian Argillite. *Journal of Geophysical Research*, *110*(B6), 1–18. https://doi.org/10.1029/2004JB003442

Revil, A., & Linde, N. (2006). Chemico-electromechanical coupling in microporous media. *Journal of Colloid and Interface Science*, *302*(2), 682–694. https://doi.org/10.1016/j.jcis.2006.06.051

Revil, A., & Mahardika, H. (2013). Coupled hydromechanical and electromagnetic disturbances in unsaturated porous materials. *Water Resources Research*, *49*(2), 1–23. https://doi.org/10.1002/wrcr.20092

Revil, A., Mahardika, H., Barnier, G., Karaoulis, M., Sava, P., Jardani, A., & Kulessa, B. (2013). Seismoelectric coupling in unsaturated porous media—Theory, petrophysics, and saturation front localization using an electroacoustic approach. *Geophysical Journal International*, *196*(2), 867–884. https://doi.org/10.1093/gji/ggt440

Richards, K., Revil, A., Jardani, A., Henderson, F., Batzle, M., & Haas, A. K. (2010). Pattern of shallow ground water flow at Mount Princeton Hot Springs, Colorado, using geoelectrical methods. *Journal of Volcanology and Geothermal Research*, *198*(1–2), 217–232. https://doi.org/10.1016/j.jvolgeores.2010.09.001

Rittgers, J. B., Revil, A., Karaoulis, M., Mooney, M. A., Slater, L. D., & Atekwana, E. A. (2013). Self-potential signals generated by the corrosion of buried metallic objects with application to contaminant plumes. *Geophysics*, *78*(5), 65–82. https://doi.org/10.1190/geo2013-0033.1

Roudsari, M. S., & Beitollahi, A. (2013). Forward modelling and inversion of self-potential anomalies caused by 2D inclined sheets. *Exploration Geophysics*, *44*(3), 176–184. https://doi.org/10.1071/EG12032

Rucker, D. F., Tsai, C.-H., Carroll, K. C., Brooks, S., Pierce, E. M., Ulery, A., & Derolph, C. (2021). Bedrock architecture, soil texture, and hyporheic zone characterization combining electrical resistivity and induced polarization imaging. *Journal of Applied Geophysics*, *188*, 1–12. https://doi.org/10.1016/j.jappgeo.2021.104306

Sharma, S. P., & Biswas, A. (2013). Interpretation of self-potential anomaly over a 2D inclined structure using very fast simulated-annealing global optimization — An insight about ambiguity. *Geophysics*, *78*(3), WB3–WB15. https://doi.org/10.1190/geo2012-0233.1

Sheffer, M. R., & Oldenburg, D. W. (2007). Three-dimensional modelling of streaming potential. *Geophysical Journal International*, *169*(3), 839–848. https://doi.org/10.1111/j.1365-246X.2007.03397.x

Shi, Y., & Eberhart, R. (1998). A modified particle swarm optimizer. In *1998 IEEE international conference on evolutionary computation proceedings* (pp. 69–73). https://doi.org/10.1109/ICEC.1998.699146

Sill, W. R. (1983). Self-potential modeling from primary flows. *Geophysics*, *48*(1), 76–86. https://doi.org/10.1190/1.1441409

Singh, A., & Biswas, A. (2016). Application of global particle swarm optimization for inversion of residual gravity anomalies over geological bodies with idealized geometries. *Natural Resources Research*, *25*(3), 297–314. https://doi.org/10.1007/s11053-015-9285-9

Soueid Ahmed, A., Jardani, A., Revil, A., & Dupont, J. P. (2013). SP2DINV—A 2D forward and inverse code for streaming potential problems. *Computers & Geosciences*, *59*, 9–16. https://doi.org/10.1016/j.cageo.2013.05.008

Srivastava, S., Datta, D., Agarwal, B. N. P., & Mehta, S. (2014). Applications of ant colony optimization in determination of source parameters from total gradient of potential fields. *Near Surface Geophysics*, *12*(3), 373–390. https://doi.org/10.1002/nsg.123001

Sundararajan, N., Rao, P. S., & Sunitha, V. (1998). An analytical method to interpret self-potential anomalies caused by 2-D inclined sheets. *Geophysics*, *63*(5), 1551–1555. https://doi.org/10.1190/1.1444451

Sungkono. (2020). An efficient global optimization method for self-potential data inversion using micro-differential evolution. *Journal of Earth System Science*, *129*(1), 1–22. https://doi.org/10.1007/s12040-020-01430-z

Sungkono, & Warnana, D. D. (2018). Black hole algorithm for determining model parameter in self-potential data. *Journal of Applied Geophysics*, *148*, 189–200. https://doi.org/10.1016/j.jappgeo.2017.11.015

Tikhonov, A. N., & Arsenin, V. Y. (1977). *Solutions of ill-posed problems*. Society for Industrial and Applied Mathematics. https://doi.org/10.1137/1021044

Tinkler, K., & Wohl, E. (1998). A primer on bedrock channels. In J. Tinkler & E. Wohl (Eds.), *Geophysical monograph series 107* (pp. 1–18). American Geophysical Union. https://doi.org/10.1029/GM107p0001

Tsai, C.-H., Rucker, D. F., Brooks, S. C., Ginn, T., & Carroll, K. C. (2022). Transient storage model parameter optimization using the simulated annealing method. *Water Resources Research*, *58*(7), 1–15. https://doi.org/10.1029/2022WR032018

Valois, R., Cousquer, Y., Schmutz, M., Pryet, A., Delbart, C., & Dupuy, A. (2018). Characterizing stream-aquifer exchanges with self-potential measurements. *Groundwater*, *56*(3), 437–450. https://doi.org/10.1111/gwat.12594

Vasconcelos, S. S., Mendonça, C. A., & Silva, N. (2014). Self-potential signals from pumping tests in laboratory experiments. *Geophysics*, *79*(6), 125–133. https://doi.org/10.1190/geo2013-0444.1

White, D. S. (1993). Perspectives on defining and delineating hyporheic zones. *Journal of the North American Benthological Society*, *12*(1), 61–69. https://doi.org/10.2307/1467686

Yuan, S., Wang, S., & Tian, N. (2009). Swarm intelligence optimization and its application in geophysical data inversion. *Applied Geophysics*, *6*(2), 166–174. https://doi.org/10.1007/s11770-009-0018-x

Yüngül, S. (1950). Interpretation of spontaneous polarization anomalies caused by spheroidal orebodies. *Geophysics*, *15*(2), 237–246. https://doi.org/10.1190/1.1437597